Additive Manufacturing 80 (2024) 103953

Contents lists available at ScienceDirect

Additive Manufacturing

journal homepage: www.elsevier.com/locate/addma

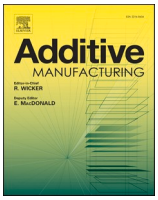

# In-process monitoring and direct simulation of Argon shielding gas and vapour dynamics to control laser-matter interaction in laser powder bed fusion additive manufacturing

Junji Shinjo [a,*], Asuka Kutsukake [a], Hideki Wakabayashi [a], Kazuto Arakawa [a], Akira Ogawara [b], Hiroyuki Uchida [c], Chinnapat Panwisawas [a,d,**], Roger C. Reed [a,e]

[a] Next Generation Tatara Co-Creation Centre (NEXTA), Shimane University, 1060 Nishikawatsu, Matsue, Shimane 690-8504, Japan
[b] NTT Data XAM Technologies Corp., 1-1-16 Fukumachi, Nishiyodogawa, Osaka 555-0034, Japan
[c] Kiguchi Technics Inc., 114-15 Enoshima-cho, Yasugi, Shimane 692-0057, Japan
[d] School of Engineering and Materials Science, Queen Mary University of London, London E1 4NS, United Kingdom
[e] Department of Materials, University of Oxford, Parks Road, Oxford OX1 3PJ, United Kingdom

ARTICLE INFO

*Keywords:*
Laser-matter interaction
Gas plume
Fume
Melt jet spatter
Argon flow dynamics

ABSTRACT

Laser powder bed fusion (L-PBF) additive manufacturing (AM) enables the fabrication of parts with precise dimensional control, freedom of design and material properties similar to or better than those fabricated using traditional manufacturing approaches. AM quality control depends upon the fundamental of the laser-matter interaction during metal AM using L-PBF to exploit the potential use of the materials and process control. In this work, thermal-fluid dynamics in gas chamber experimentally and computationally is used to elucidate the interplay between vapour, liquid, and solid phases in L-PBF. It is revealed that the argon (Ar) shielding gas flow with varied inlet velocities by different nozzles has a pronounced effect to minimise the laser-fume interaction, resulting in the reduction in unstable metal vapour flow and enhancing laser absorptivity. In-process monitoring via high-speed visualisation has been used to understand the simultaneous gas plume dynamics as a result of vapourisation and subsequent laser-fume interaction, backed up by thermal-fluid flow simulation. Unfavourable process dynamics associated with unwanted defects such as lack of fusion can be avoided to improve process design and enhance process stability.

## 1. Introduction

Additive manufacturing (AM) is an emerging digital fabrication technology that can enable to manufacture complicated parts with a high degree of freedom. Especially, metal AM is considered to be promising in manufacturing temperature-resistant superalloy parts for aerospace and automotive applications with precise composition and process control. There have been numerous studies in the chamber scale [1–8] or in the melt pool scale [9–26] to seek optimised process conditions to assure good product quality. Comprehensive review on melt pool scale phenomena can be found in [27,28].

There are various interfacial phenomena and physical processes involved in metal AM, such as laser heating, partial or full powder melting, thermal fluid flow motion in the melt pool, vapourisation, heat transfer to the surrounding layers and finally rapid solidification. From the hot melt pool, evaporated gas can be generated and induces an upward 'plume' (vapour), which may contain 'fume' (solid nano-particles) generated by condensation of the vapour. Due to the evaporative gas flow, hot spatter particles (partly melt particles) may be also ejected from the melt pool and cold powders in the vicinity may be entrained as well [9–27]. These phenomena make the metal AM complicated, and the final product quality is strongly dependent on the process conditions and processing window.

As described above, one of the factors affecting the AM product quality in the fabrication chamber is the ejected vapour gas, fume and spatter particles. They interact with the laser beam and may hinder sufficient heating necessary for the fabrication. Typically, shielding gas such as Argon is used to blow away the fume and spatter particles from

* Corresponding author.
** Corresponding author at: School of Engineering and Materials Science, Queen Mary University of London, London E1 4NS, United Kingdom.
*E-mail addresses:* jshinjo@ecs.shimane-u.ac.jp (J. Shinjo), c.panwisawas@qmul.ac.uk (C. Panwisawas).

https://doi.org/10.1016/j.addma.2023.103953
Received 8 September 2023; Received in revised form 21 December 2023; Accepted 31 December 2023
Available online 4 January 2024

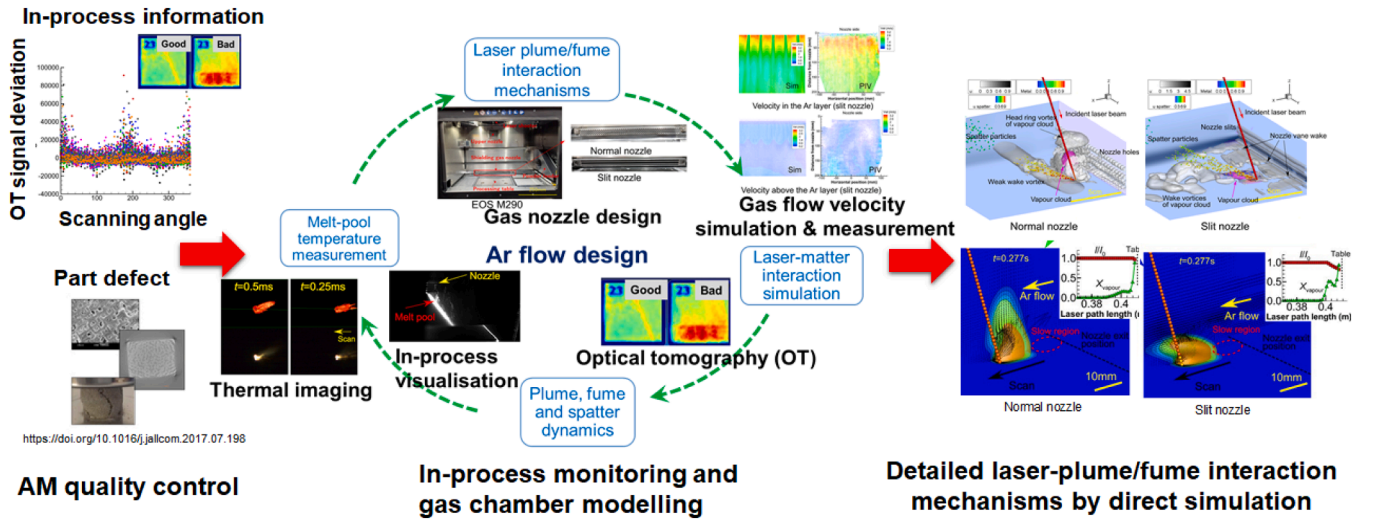


**Fig. 1.** Schematic diagram of the research outline. Motivated by industrial issues of quality control, in-process monitoring is conducted for gas chamber modelling and the over-arching aim is to elucidate detailed laser-plume/fume interaction mechanisms by direct simulation.

the processing region. Still, even under the same process conditions, the final melting and solidification quality may differ by the location inside the processing chamber [4]. The scanning direction may also affect the part quality [28]. These suggest that the flow non-uniformity in the chamber affects the AM process, and the shielding gas flow design should be carefully done. This is critical especially in the industrial production and therefore it is significantly important to control the shielding gas flow in the processing chamber. However, detailed laser interaction has not been well understood and its process improvement has not been done in an integrated way in a processing chamber, which has motivated the present study.

Several studies have been conducted on laser-fume or laser-spatter interaction in the fabrication chamber in which the laser beam is scattered or absorbed and insufficient melting occurs. In the chamber-scale studies, the shielding gas flow field has been mainly investigated [1–8]. Ferrar *et al.* [1] studied the flow in a chamber by simplified computational fluid dynamics (CFD) and compared with experimentally observed porosity, and found that the flow uniformity is important for quality assurance. Ladewig *et al.* [2] investigated the surface roughness, lack of fusion and powder re-deposition in L-PBF AM and proposed several mechanisms of laser attenuation such as laser scattering by fume, insufficient melting and subsequent balling. Reijonen *et al.* [3] experimentally measured the shielding gas flow in an L-PBF chamber and confirmed the significance of the shielding gas effect. Tenbrock *et al.* [4] also investigated the plume gas distribution and identified the degree of laser-plume interaction in the affected region. Elkins *et al.* [5] measured the gas flow velocity field in EOS M290 machine, which is also the target machine in this study, and suggested the correlation with the shielding gas flow and the processing quality. Snow *et al.* [6] experimentally investigated the spatter ejection and the degree of lack of fusion and confirmed a strong correlation between them.

Studies on the spatter trajectories also exist. Zhang *et al.* [7] simulated the flow field in a chamber and tracked the trajectories of spatter particles. They also proposed a new inlet design to minimise the Coanda effect for a better spatter removal efficiency. Chien *et al.* [8] also simulated the gas flow and spatter particles and showed the effectiveness of simulation in predicting the spatter trajectories in a commercial chamber.

To improve the modelling accuracy, experimental visualisation efforts in the near melt pool region have been continued. Ye *et al.* [11] used experimental data to calibrate the absorptivity including fume-laser interaction. Zheng *et al.* [10,13] clarified the vapour plume and spatter direction. The plume is inclined toward the backward direction of the scan direction and the inclination angle is different under several process conditions. Bidare *et al.* [14,15], Guo *et al.* [16], Gunenthiram *et al.* [17], Young *et al.* [18], Yin *et al.* [20,21], Bitharas *et al.* [19,22] gave detailed experimental observations of plume and spatter velocity and direction in the near melt pool region. Similarly, in numerical simulation [23–26], the spatter dynamics has been discussed in the near field. These data in the near field scale should be connected to the chamber scale to fully understand the AM process. Liu *et al.* [27] and Li *et al.* [28] give comprehensive reviews on the spatter/vapour dynamics and laser interaction. In spite of these efforts, a thorough understanding on laser-fume and laser-spatter interaction needs more studies and analyses. Especially, direct laser-spatter and laser-fume interaction in a chamber scale and the correlation with subsequent incomplete fabrication characteristics have not been explored in detail.

In the course toward such a goal, the present study aims to directly reveal the effect of laser-fume and laser-spatter interaction in chamber-scale AM and obtain insights for a better process condition setup, using both experimental data and numerical simulation. Fig. 1 schematically shows the research scope of the present study. Motivated by industrial issues of quality control, in-process monitoring is conducted for gas chamber modelling and detailed laser-plume/fume interaction mechanisms will be clarified by direct simulation. In the simulation, laser ray tracking is utilised with absorption and scattering due to fume and spatter particles. Vapour/spatter distribution is identified and the variation of laser heat absorption by the scanning angle difference is investigated. To the best of our knowledge, investigating the process quality by directly solving the vapour/spatter distribution and tracking the laser interaction in an AM chamber is the first one. In fact, Bitharas *et al.* [22] pointed out that laser beam often interacts with the ejected vapour and condensate, but this effect is mostly overlooked and including the effects in numerical models could greatly enhance the predictive capability, allowing a priori identification of process quality. In a series of our experiments, data have been obtained such as the gas velocity field by particle image velocimetry (PIV), spatter trajectories by high-speed camera imaging, the melt pool temperature by thermal imaging, heat absorption by optical tomography (OT) imaging, and the final product quality after fabrication. These datasets are used combined with the CFD simulation. This study will also give insights into the future research direction towards a further understanding on the phenomena in the plume vapour where the gas phase, the condensed nano-particle solid phase and the laser interact in a complicated way.

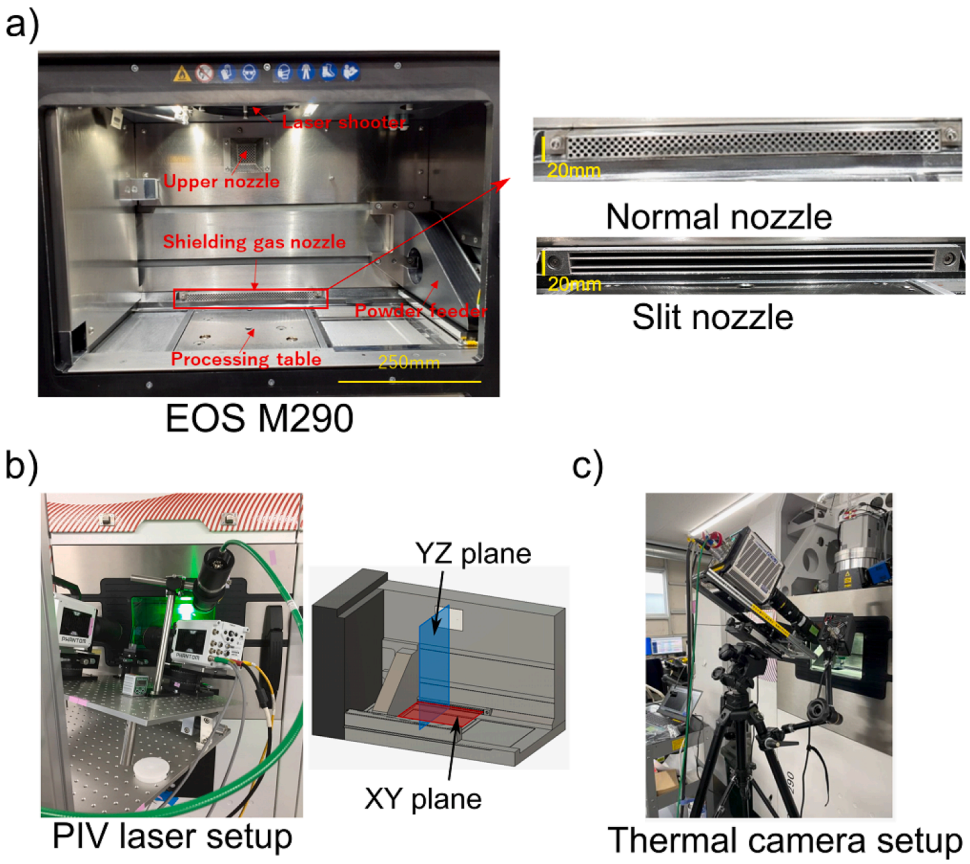


**Fig. 2.** The processing chamber of EOS M290. (a) Photo of the processing chamber and nozzles, (b) camera and laser setup for PIV measurement and (c) thermal camera setup for temperature measurement.

**Table 1**
Chemical compositions of EOS IN718 [30] (weight %).

| Elements | Fe | Ni | Cr | Nb | Mo | Ti | Al | Co | Cu | Si |
|---|---|---|---|---|---|---|---|---|---|---|
| max | Rem. | 55.00 | 21.00 | 5.50 | 3.30 | 1.15 | 0.80 | 1.00 | 0.30 | 0.35 |
| min | | 50.00 | 17.00 | 4.75 | 2.80 | 0.65 | 0.20 | - | - | - |

| Elements | Mn | Ta | C | S | P | B | Pb | Se | Bi |
|---|---|---|---|---|---|---|---|---|---|
| max | 0.35 | 0.05 | 0.08 | 0.015 | 0.015 | 0.006 | 0.0005 | 0.0020 | 0.00003 |
| min | - | - | - | - | - | - | - | - | - |

## 2. Methods

### 2.1. Experimental visualisation

The processing machine used in this study is M290 (EOS GmbH) [29] for L-PBF. The picture of the whole processing chamber is shown in Fig. 2a. The processing table size is 250 mm × 250 mm. Before the processing table, a nozzle is attached to control the shielding gas flow. Fig. 2a shows the "normal" nozzle where many holes are attached for incoming shielding gas (Ar) and a new "slit" nozzle where the inlet shape is changed to three horizontal slits. The concept of the new slit nozzle is to reduce the gap between the building plate surface and the lower edge of the nozzle exit, suppressing the Coanda effect (deflection of the shielding gas flow toward the building plate) [7]. If the gap is too small, the shielding gas then tends to blow the powders off the building plate. Therefore, the balance is important and the gap height as small as 2 mm is taken here. The new nozzle design has proved better performance than the normal nozzle as discussed later in **4.1.1**. The square-like nozzle in the upper-front (upper nozzle in Fig. 2a) is to suppress the soaring powders and fume to prevent contamination on the laser protection glass. The laser is shot from the ceiling part over the processing table. The powder feeder (currently in the far right) is located in far left when the laser processing is taking place. The material used here is Ni-based superalloy IN718 by EOS GmbH (Germany). The compositions of the powders are shown in Table 1 [30].

**A) Optical tomography (OT) measurement**

The optical tomography (OT) signal is measured by EOSTATE Exposure OT (EOS GmbH, Germany). It measures near infrared (NIR) signal by an sCMOS camera. As later shown, the signal intensity has a correlation with the processing quality.

**B) Particle image velocimetry (PIV) for velocity field and Cassegrain imaging for spatter**

PIV is a method to extract the velocity vector by introducing small seed particles in the flow field and comparing two images between a very short time interval. The high-speed camera used in this experiment is Phantom T1340 (Vision Research Inc., USA) and the frame rate is 1,000-13,000fps. Seeding is done by PIVpart14 (PIVTEC GmbH, Germany). The velocity vector extraction is done by Koncerto II software (Seika Digital Image Corp., Japan). The viewing planes are set both in vertical and horizontal directions (Fig. 2b). Spatter particle spontaneous

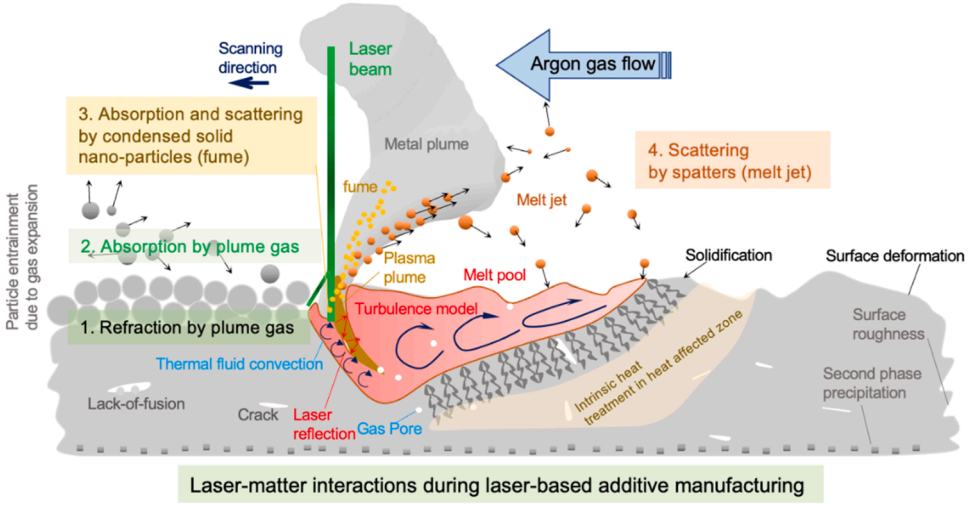


**Fig. 3.** Schematic of phenomena relative to L-PBF AM. This is for an example case of laser scanning parallel to the Ar shielding gas flow (after [34]).

emission is measured in a combination with Cassegrain imaging by Maksutov-Cassegrain optical system (Seika Digital Image Corp., Japan).

**C) High-speed camera imaging in the vicinity of melt pool**

The melt pool temperature is measured by two-colour method, where the ratio of two infrared rays at different wavelengths is used to identify the temperature. The high-speed camera for this measurement is MEMRECAM ACS-1 (NAC Image Technology, Japan) whose frame rate is 100,000 fps with 1280 × 448 pixel resolution. The temperature calibration is done by the standard heat source LSB-1NC (Tsubosaka Electric Co., Ltd., Japan). For high-speed imaging (Supplementary Video 3), the LED light source is UFLS-751 (NAC Image Technology, Japan) whose brightness is 3500 lm and its correlated colour temperature is 6000–8500 K. The primary aim of this imaging is to have input information for simulation on spatter size, direction, velocity and vapour gas velocity. The motion of hot spatter particles can be seen by self-luminescence and cold spatters can be also seen by illumination near the melt pool although they are relatively much darker. The spatter velocity of small particles, hot or cold, can be assumed to be identical to the velocity of vapour gas which entrains them [28]. Therefore, later in estimating the vapour gas velocity, motion of hot spatter particles is utilised (**4.1.2 (c)**). Fig. 2c shows the camera setup.

### 2.2. Numerical simulation

For brevity, details of the governing equations for the gas phase fluid dynamics and particle dynamics (**A)** and **B)** below) are given in **Appendix A) and B)**.

**A) Shielding gas, vapour dynamics and turbulence equations**

The numerical simulation is conducted based on the computational fluid dynamics (CFD) approach. As will be discussed in Section 3., the horizontal grid resolution is not small enough to resolve the melt pool. Therefore, the melt pool conditions are given as model boundary conditions (see **4.1.2**). Similarly, unresolved sub-grid scale (SGS) turbulence eddies are modelled in the framework of large eddy simulation (LES).

The governing equations for the chamber gas flow are the conservation of mass, momentum, energy and species concentration, including particle tracking [31] and laser Ray tracing. These equations are formulated in the LES context and the unclosed SGS turbulence terms are modelled by the Smagorinsky model [32]. The numerical scheme is based on a total-variance diminishing (TVD) scheme using Chakravarthy-Osher's limiter [33]. The viscous and diffusion terms are formulated by the 2nd-order central differencing. Further remarks on code validity are given in **Appendix C)**.

**B) Particle equations**

Ejected spatter particles are tracked as point-particles in the Lagrangian framework. Particle motion, heat transfer and evaporation are considered. Collision between spatter particles is not considered here. The particle effects are two-way coupled with the flow field. The particle equations are numerically solved using the 4th-order Runge-Kutta time integration.

**C) Integrated absorption and scattering modelling: Vapour plume refraction, vapour plume absorption, fume nano-particle scattering and absorption, and spatter particle scattering**

Laser ray tracing is conducted to track the laser trajectories. Here, utilising the point particle methodology, many virtual energetic photons are injected from the laser source position and the motion of each photon particle is tracked. Once the photon reaches the solid or liquid surface, part of the energy of the photon is deposited and the photon will be reflected, assuming diffusive reflection. After multiple reflections when the contained energy is small enough, ray tracing is stopped.

For the melt pool, experimental results in **4.1** are incorporated. The vapour gas is ejected from the melt pool upward and backward (relative to the scanning direction), with some inclined angle. This angle is almost the same as the spatter angle as shown in **4.1.2**. The ejection velocity is estimated by the PIV and video measurement results in **4.1.2**. Spatter particles are similarly ejected from the melt pool location. The particle size, ejection velocity, ejection angle and ejection frequency are given with some added randomness to mimic the experimental results in **4.1.2**.

To newly include gas-laser interaction and particle-laser interaction, the following models are examined, (1) **refraction by plume gas**, (2) **absorption by plume gas**, (3) **absorption and scattering by condensed solid nano-particles (fume)** and (4) **scattering by spatter particles (melt jet)**. Fig. 3 shows these phenomena schematically. Note that the metal plume (vapour) may be deflected by the shielding gas flow and may interact with the incident laser beam.

The effect of refraction due to the vapour plume (effect 1) is considered to be minor for the temperature below 6000 K since the refractive index for the 1070 nm laser does not change much [9]. In fact, the temperature measurement indicates that the plume temperature is ~3200 K at maximum in the present study (later shown in **4.1**). Therefore, this effect is neglected.

The effect of absorption due to the vapour plume plasma (effect 2) is called the inverse Bremsstrahlung absorption [9,35,36]. Using an approximated formulation in [36], the absorption coefficient can be obtained by

$$K \approx 3.3 \times 10^{-41} N_e^{\,2} T_e^{\,-\frac{3}{2}} \tag{1}$$

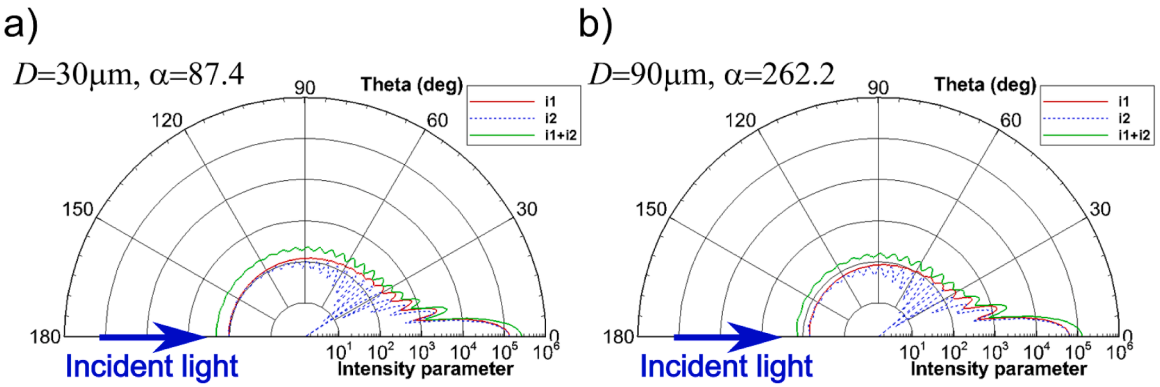


**Fig. 4.** Mie scattering characteristics for large spatter particles. $i_1 = |S_1|^2$ and $i_2 = |S_2|^2$.

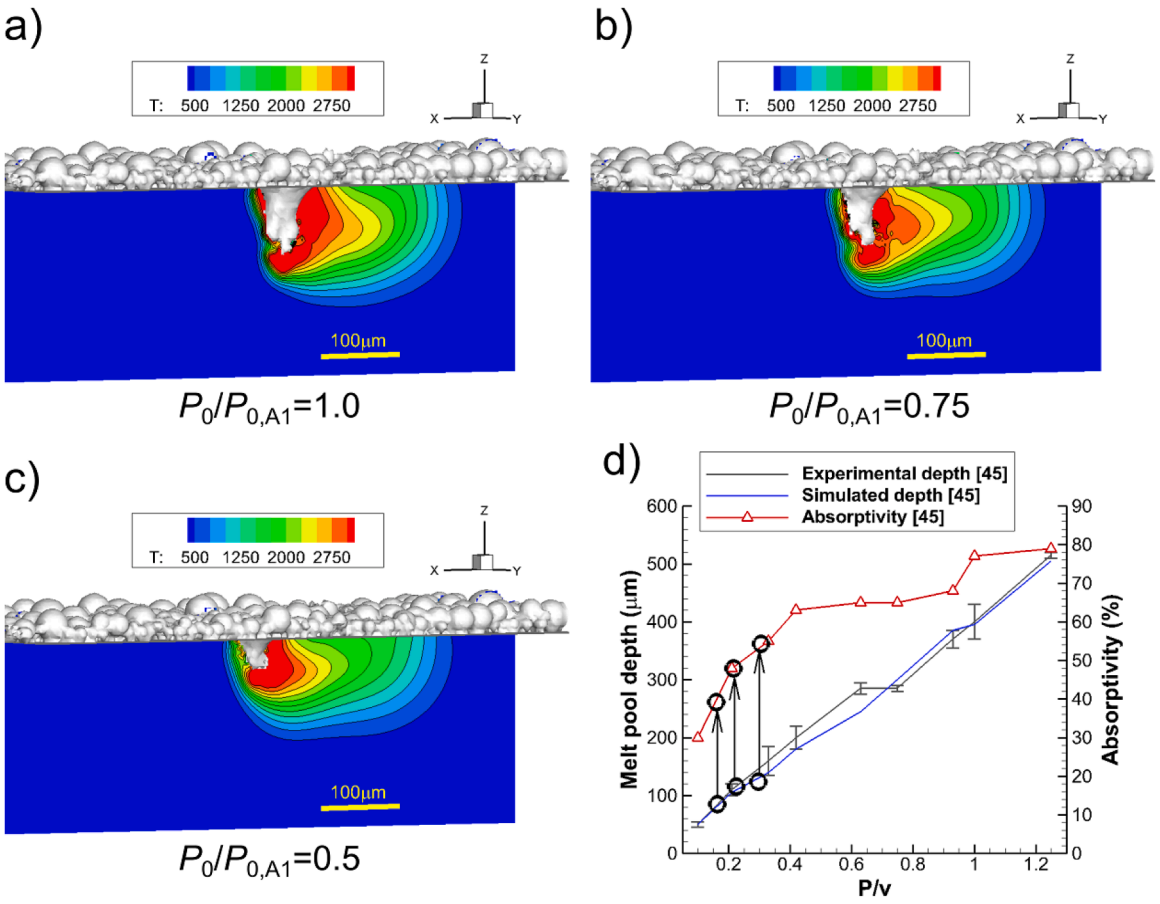


**Fig. 5.** Melt pool depth against the overall power input. Data are taken from [45]. (a)-(c) Simulated temperature result. (d) The surface absorptivity obtained by this figure.

where $N_e$ is the electron density ($m^{-3}$) $T_e$ is the electron temperature (K) and the absorption coefficient $K$ is in $m^{-1}$. Even using large values of $N_e$ and $T_e$, the absorption by the Lambert-Beer law gives less than 1% of absorption for $x = 10$ mm plume length. Therefore, the effect of inverse Bremsstrahlung absorption can be neglected. This is consistent with the estimation of [9].

Laser-particle interaction (effect 3 and effect 4) is characterised by scattering and absorption. The particle parameter is defined as

$$\alpha = \frac{2\pi a}{\lambda} \tag{2}$$

where $a$ is the particle radius and $\lambda$ is the laser wavelength. If $\alpha \ll 1$, Rayleigh scattering [37,38] occurs, which corresponds to scattering and absorption due to nano-condensation particles (effect 3). If $\alpha$ is a mid-range value such as $O(\alpha) \sim 10$, Mie scattering [39] occurs, which corresponds to scattering due to spatter particles (effect 4). Note that if $\alpha \gg 1$, it reduces to geometrical reflection.

For the Rayleigh scattering of O(10–100 nm) particles in the plume (effect 3), the absorption and scattering coefficients are given by [9,38].

$$K_{abs} = \frac{4\pi a}{\lambda}\mathrm{Im}\left(\frac{m^2-1}{m^2+2}\right)n_d\pi a^2$$
$$K_{sca} = \frac{8}{3}\left(\frac{\pi a}{\lambda}\right)^4\left|\frac{m^2-1}{m^2+2}\right|^2 n_d\pi a^2 \tag{3}$$

**Table 2**
Cases for determining absorptivity and attenuation factor.

| Case | Overall input laser energy (W) | Laser scanning velocity (mm/s) | Laser spot diameter (μm) |
|---|---|---|---|
| A1 | 285 | 1000 | 80 |
| A2 | 285 × 0.75 | 1000 | 80 |
| A3 | 285 × 0.5 | 1000 | 80 |

where $n_d$ is the number density and $m$ ($= n + ik$) is the complex refractive index. The ratio of scattering to absorption for $r = 50$ nm nano-particles of Ni ($m = 1.9648 + 3.8352i$) makes $K_{sca}/K_{abs} \sim 0.017$, which means that scattering effect can be relatively small [9].

This is still an open question, and Reijonen *et al.* [3] claims that the above estimation is for relatively large-scale welding and the scattering effect should be larger (~10% or more) for small-scale melt pool in AM. It is also argued that agglomeration of condensed nano-particles may happen and these larger particles induce more scattering. These are not fully confirmed quantitatively, but reasonably possible. Since detailed physical analysis of these complicated nano-particle-driven phenomena is beyond the scope of the present study, the overall effect of nano-particle-driven scattering and absorption is expressed in the form of Lambert-Beer law

$$I = I_0 \exp\left(-KX_{vapour}x\right) \tag{4}$$

where $X_{vapour}$ is the vapour molar fraction and the overall attenuation factor $K$ is fitted to the experimental results (see **D)**).

For Mie scattering due to spatter particles (effect 4), the scattered light intensity is given by [39,40].

$$I = I_0\left(\frac{1}{kr}\right)^2 \frac{1}{2}\left(|S_1|^2 + |S_2|^2\right)$$
$$S_1 = \sum_n \frac{2n+1}{n(n+1)}\left(a_n\pi_n + b_n\tau_n\right) \tag{5}$$
$$S_2 = \sum_n \frac{2n+1}{n(n+1)}\left(a_n\tau_n + b_n\pi_n\right)$$

where $k$ is the laser wave number and $r$ is the distance from the particle. $a_n$, $\pi_n$, $b_n$ and $\tau_n$ are comprised by Bessel functions. The scattering direction is more forward-oriented as the particle parameter gets larger. To calculate Mie scattering, the program code BHMIE developed by Bohren and Huffman [40] is used in this study. Fig. 4a,b shows examples for the diameter of $D$= 30 μm and 90 μm. The light is almost scattered to the front with some angle band. In this study, for each photon which collides with a spatter particle, the scattering angle is stochastically varied while statistically satisfying the angle range predicted in Fig. 4.

It is also noted by Ye *et al.* [11] and Khairallah *et al.* [12] that reflection from the melted surface is different between the conduction mode and keyhole mode. In the conduction mode, the melted surface is rather flat and laser reflection is mostly once or twice. Therefore, the reflected outgoing rays have not reduced the energy much. In contrast, in the keyhole mode, the number of reflection inside the keyhole increases and as a consequence the reflected outgoing rays have smaller energy. In some of our experiments, the top view OT imaging may capture a rather larger and brighter melt pool spot for the conduction mode due to this reflection energy difference. This factor is also interesting to simulate in detail, but again considering the main objective of shielding gas flow design in the present study, this is left for a future study by detailed numerical simulation.

**D) Simulation of melt pool scale melting to determine the overall attenuation coefficient *K***

In order to determine the overall attenuation coefficient $K$ in Eq. (4), several preliminary cases are simulated using our TATM-MEX code [41–44]. This code is tuned to conduct melt pool scale detailed simulation in AM and enables to solve solid-liquid-gas phase transition with laser ray tracing. The details of the formulations and the code structures can be found elsewhere [41–44], with some validation cases of the code.

Instead of directly including the laser attenuation due to the vapour, virtually the overall laser energy input is varied. Using the simulation results of melt pool depth (Fig. 5) and reference data by Khorasani *et al.* [45], $K$ is determined by the post-simulation analysis as follows.

The effective overall laser input is varied as shown in Table 2. Case A1 is the reference case where the laser ray attenuation is assumed to be zero. To correlate the melt pool depth with the laser ray attenuation, two more cases varying the effective laser power, namely $r_a\eta$, the product of laser ray attenuation ratio $r_a$=$I/I_0$ and the powder surface absorptivity $\eta$, is examined. $I_0$ is the laser intensity at the start of the laser ray and $I$ is the intensity after passing through the fume/plume. (Hereafter, the melt pool surface area is assumed unchanged. Therefore, $I/I_0 = P/P_0$ where $P$ is the laser power and the subscript 0 denotes the start of the laser ray.) The surface absorptivity $\eta$ is taken from Khorasani *et al.* [45], in which they determined $\eta$ for IN718 by calibrating the value to fit the experimental melt pool depth. Their heat model in the simulation is based on the assumed surface/volumetric heat model [46], and the effect of laser ray attenuation was not directly included ($r_a$=1) but the overall effect was put in the absorptivity. Taking advantage of this $r_a$= 1 assumption, we decompose the overall energy attenuation into the laser ray attenuation and the variation of surface absorptivity due to power input.

To determine the laser ray attenuation, "overall input laser energy" in Table 2, or the *total* deposited laser power to the surface, is virtually varied in the present simulation (Cases A1 to A3) and the melt pool depth is compared with the measured melt pool depth of Khorasani *et al.* [45]. Namely, $P_0/P_{0,A1}$= 1.0, 0.75 and 0.5 (where $P_{0,A1}$=285 W) are considered as a source laser power. Since the *total* energy given to the surface is the key, in this simulation the laser ray attenuation is set zero, and in the post-simulation analysis the variation of the overall energy ($P_0/P_{0,A1}$) is decomposed into the laser ray attenuation and the variation in the surface absorptivity $\eta$. The analysis is done in the following steps.

(1) The overall energy deposited onto surface $P_0/P_{0,A1}$ is set (1.0, 0.75 and 0.5).

(2) Conduct three simulation cases without considering ray attenuation and using the same $\eta_{A1}$= 0.55.

(3) Confirm that the melt pool depth for each case is reproduced similarly as in Khorasani *et al.* [45]. (It is also confirmed by our experimental data).

(4) Choose $\eta$ from Fig. 5d for $P_0/P_{0,A1}$= 0.75 and 0.5.

**Table 3**
Laser ray attenuation ratio obtained by analysis of simulation data.

| Case | Ratio of overall energy deposited onto surface $(r_a{\cdot}\eta)/(r_a{\cdot}\eta)_{A1} = P_0/P_{0,A1}$ | Effective laser power/scanning speed (W/ (mm/s)) $= P/v$ | Simulation result of melt pool depth (μm) | $\eta$ from Khorasani *et al.* [45] by the effective laser power/scanning speed | Laser ray attenuation *relative* to A1 $(r_a)/(r_a)_{A1}$ |
|---|---|---|---|---|---|
| A1 | 1.0 | 0.285 × 1.0 = 0.285 | 120 | 0.55 ($= \eta_{A1}$) | 1.0 (reference) |
| A2 | 0.75 | 0.285 × 0.75 = 0.214 | 105 | 0.46 | 0.90 |
| A3 | 0.5 | 0.285 × 0.5 = 0.143 | 90 | 0.38 | 0.72 |

**Table 4**
Case setup.

| Case | Shielding gas nozzle | Laser power (W) | Laser scanning velocity (mm/s) | Laser spot diameter (μm) | Laser scanning direction with respect to shielding gas flow | Processing location in Fig. 6b |
|---|---|---|---|---|---|---|
| B1 | slit | 285 | 960 | 80 | parallel | A |
| B2 | slit | 285 | 960 | 80 | parallel | B |
| B3 | normal | 285 | 960 | 80 | parallel | A |
| B4 | normal | 285 | 960 | 80 | parallel | B |
| C1 | slit | 285 | 960 | 80 | perpendicular | A |
| C2 | slit | 285 | 960 | 80 | perpendicular | B |
| C3 | normal | 285 | 960 | 80 | perpendicular | A |
| C4 | normal | 285 | 960 | 80 | perpendicular | B |

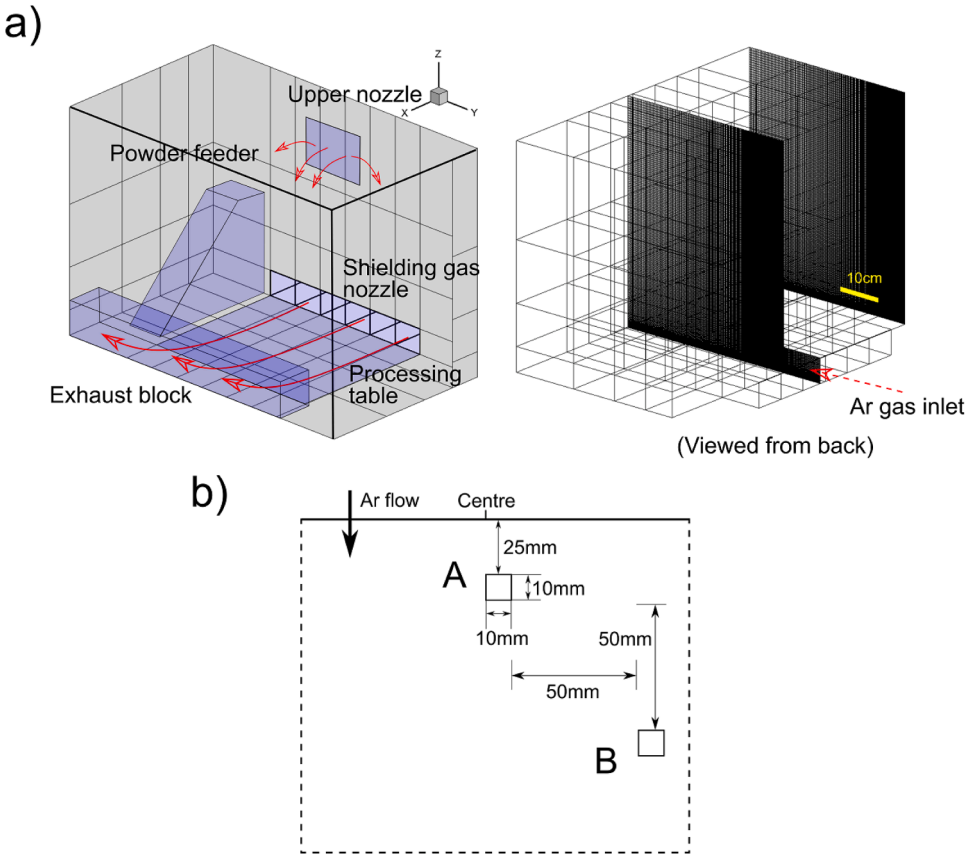


**Fig. 6.** (a) Schematic illustration of computational domain and grid system (viewed from back) and (b) the processing locations. The position A is at the centre of the table in the transverse direction and 25 mm downstream from the nozzle exit. The position B is at + 50 mm in the transverse direction and + 50 mm downstream relative to A.

(5) By the above $\eta$, estimate the laser ray attenuation assuming that the reduced $P_0/P_{0,A1}$ (=0.75 and 0.5) is due to the multiplication of $\eta$ and the laser ray attenuation ratio.

Fig. 5a,b,c shows the temperature distribution and the simulated melt pool depth is plotted in Fig. 5d with the data from Khorasani *et al.* [45]. For this calculation, the grid resolution is set as 4 μm, which is sufficiently fine to resolve the powder-scale phenomena. The simulated melt pool depth is in good agreement with the experimental data of Khorasani *et al.* [45]. (The depth is also in agreement with our experimental data). Then the corresponding $\eta$ value is read from the solid red curve in Fig. 5d. To obtain the laser ray attenuation *relative* to Case A1 (with $\eta_{A1}$=0.55), the relative laser ray attenuation can be estimated as 0.90 and 0.72 for Cases A2 and A3, respectively. Table 3 summarises the results, in which the three columns in the right hand side are determined by the present simulation cases. It should be noted again that the total energy to the powder surface is determined by $r_a\eta$.

The relative variation $(r_a)/(r_a)_{A1}$ in the rightmost column indicates the pure laser attenuation effect, which is used to fit the $K$ value in the Lambert-Beer formulation (Eq. (4)). Using the laser path length $x$ and the vapour distribution $X_{vapour}$ from the calculated flow field of Fig. 5a,b,c the pure laser ray attenuation $(r_a)/(r_a)_{A1}$ is fitted and the obtained value is $K$= 50 $m^{-1}$. Using this attenuation coefficient, the laser-fume interaction will be discussed more in detail in **4.2.** It should be noted again that direct laser hit on a spatter particle and resultant scattering is considered as a different process, as explained in **C)**.

## 3. Processing case setup

The experimental nominal processing conditions are the laser power of 285 W, the scanning velocity of 960 mm/s, the laser spot diameter of 80 μm and the powder layer thickness of 40 μm. The powder size is $D_{10}$ = 18.0 μm, $D_{50}$ = 32.1 μm, and $D_{90}$ = 54.2 μm. For this study, 10 mm × 10 mm cube shape is fabricated, varying the scan direction and the processing location. Table 4 summarises the processing

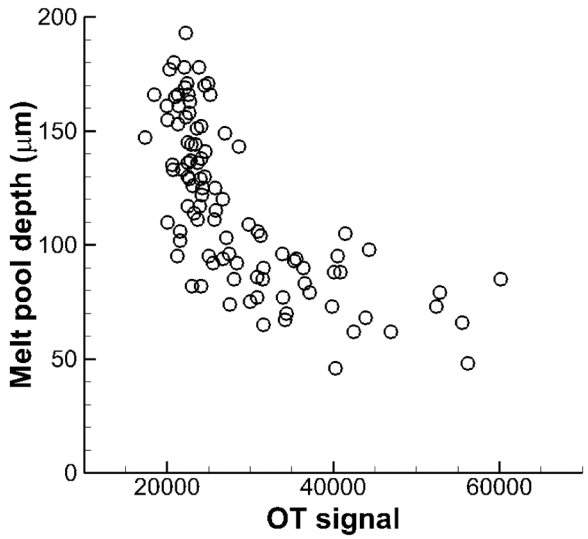


**Fig. 7.** Experimental correlation between the OT signal and melt pool depth.

parameters in the present study.

Fig. 6a shows the computational domain and the grid system. The upstream part of the shielding gas nozzle block is connected to the chamber. The exit duct sucks the flow out of the chamber. Fig. 6b shows the processing locations. The position A is at the centre of the table in the transverse direction and 25 mm downstream from the nozzle exit. The position B is at + 50 mm in the transverse direction and + 50 mm downstream relative to A. The computational grid resolution is 1 mm in the horizontal direction and the minimum grid resolution at the table wall is 0.35 mm. This resolution is not sufficient enough to resolve the turbulent boundary layer and the LES subgrid model is used as described in **2.2**. The chamber walls are treated as non-slip walls. The inlet total pressure is set from the experimental PIV velocity data at the nozzle exit. The powder feeder is included in the domain, assuming as an immersed-boundary body. The domain is decomposed into 134 subdomains and the total number of grid points is 28.9 million. The CFL number of 0.25 is used and the cold flow field development is first calculated for two flow-through times in the chamber (~8.25 million time steps), and then hot laser processing is started.

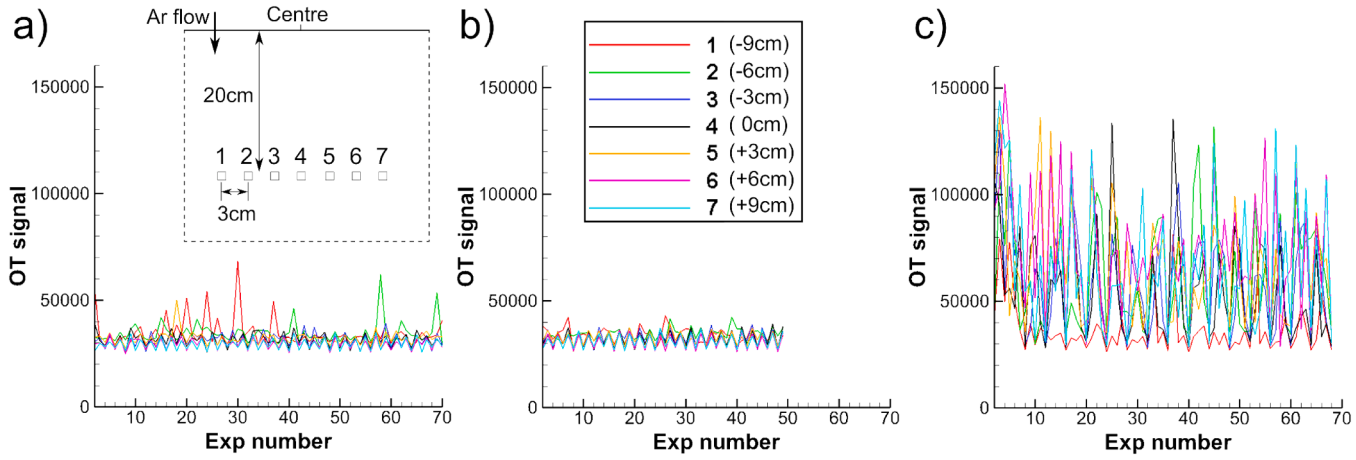


**Fig. 8.** Measured OT signals. The measurement points 1–7 are located 20 cm downstream of the nozzle. The lateral position relative to the centre of the nozzle is − 9 cm, − 6 cm, − 3 cm, 0 cm (centre), + 3 cm, + 6 cm, + 9 cm for point 1, 2, 3, 4, 5, 6 and 7, respectively. "Exp number" denotes the consecutive number of experiments. (a) Measurement with the normal nozzle, (b) measurement with the slit nozzle and (c) measurement with the normal nozzle under intentionally reduced Ar gas flow condition.

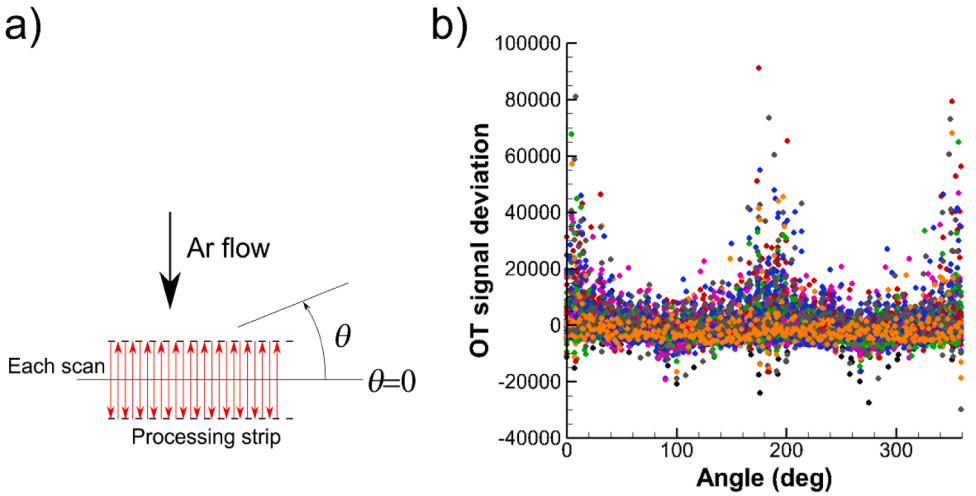


**Fig. 9.** Effect of scanning angle on OT signals. (a) Definition of angle. Here $\theta$ is the angle of processing strip direction (black line). The scanning direction is normal to $\theta$ (red arrows), (b) dependence of OT signal deviation on the scanning angle. Different colours mean different cases.

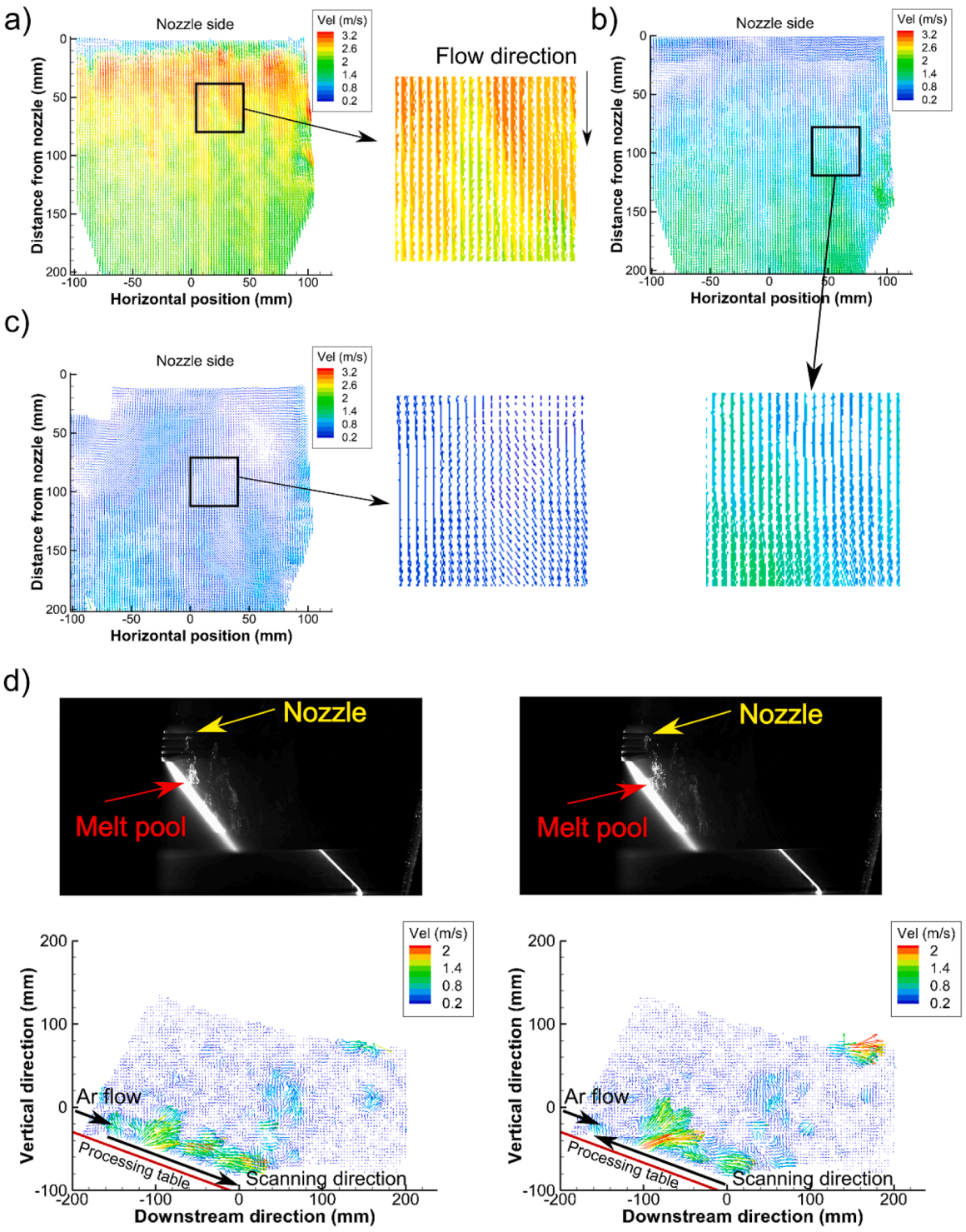


**Fig. 10.** Flow velocity measurement by PIV. (a) 10 mm height XY plane, (b) 20 mm height XY plane and (c) 30 mm height XY plane. (d) Hot processing case on YZ plane. The images are inclined due to the limitation of the experimental viewing angle. (See **Supplementary Video 1**).

## 4. Results and discussion

### *4.1. Experimental measurements*

In order to understand the correlation between optical signal and the processing quality, experimental measurements are analysed in **4.1.1**. There are fluctuations in the processing quality, which implies that there is some correlation with the shielding gas parameters such as the gas velocity and the relative gas direction. Questions are raised by these trends as to what factors are causing the laser interaction, and these questions are investigated by numerical simulation in **4.2.** Subsection **4.1.2** aims to acquire data especially near the melt pool region so that the boundary conditions for simulation can be obtained.

#### *4.1.1. Overview of processing: optical tomography signal and processing quality*

The OT signal can be correlated with laser heat. In this study, the relative trends of OT signals are compared. Fig. 7 shows the

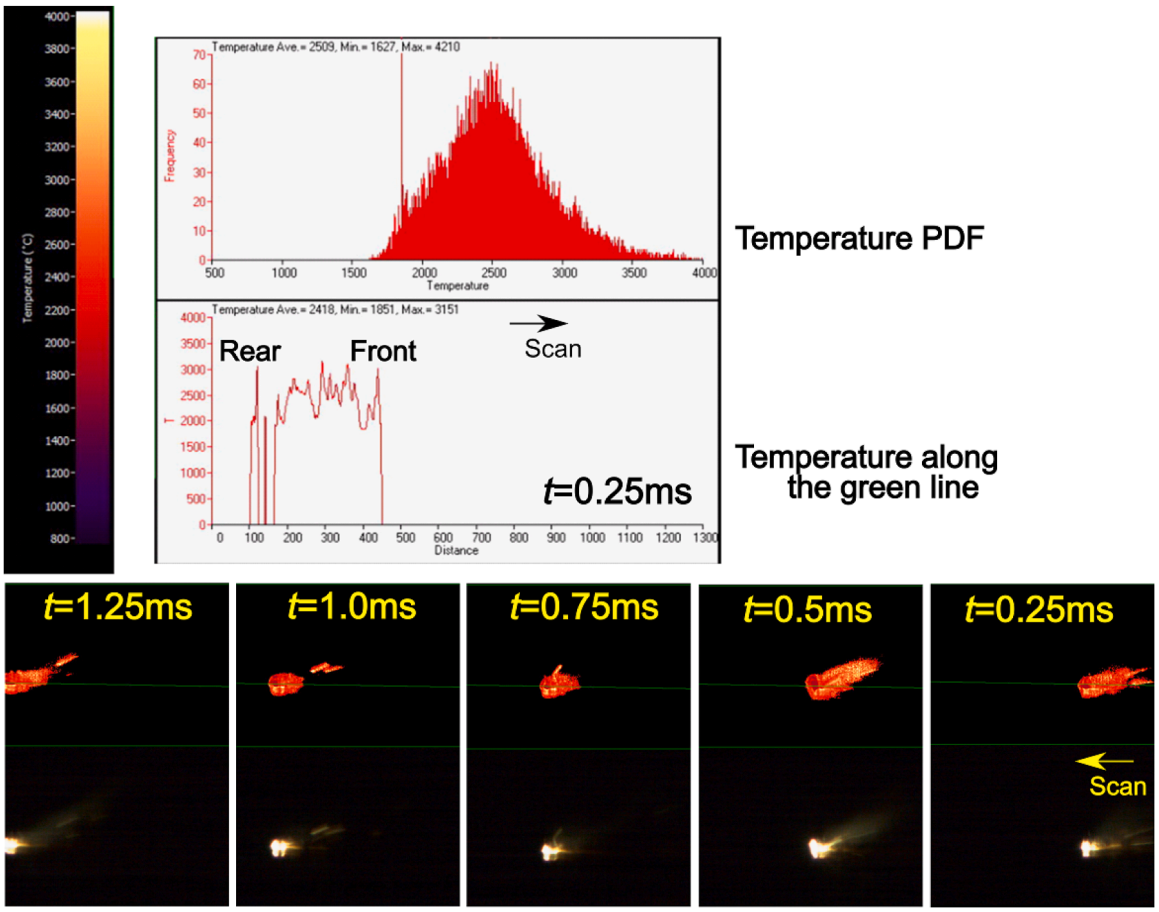


**Fig. 11.** Temperature measurement by thermal imaging. The temperature is in deg C. In each time frame photo, the lower half is a visible image and the upper half is a thermal image. The insert indicates the temperature PDF and the temperature distribution along the green line at $t = 0.25$ ms. (See **Supplementary Video 2**).

experimental correlation of OT signal and melt pool depth using the normal nozzle for the nominal processing conditions. Even for the same process conditions, the melt pool depth has a range of variation. Therefore, it implies that there should be a factor which determines the degree of melting, i.e. the absorbed energy, other than the preset energy density. There is a trend that the larger OT signal means the shallower melt pool. When the heat absorption is larger (smaller OT signal), it is expected to be in the keyhole mode and therefore the emitted ray strength is weaker. In contrast, when the heat absorption is smaller (larger OT signal), the melt pool is shallower as it is expected to be in the conduction mode.

Fig. 8 shows the effect of shielding gas nozzle on the OT signal. The measured locations (1−7) are put at 20 cm downstream of the nozzle with 3 cm interval in the horizontal direction. Using the normal nozzle, there are some deviations in the OT signal (Fig. 8a), while this variation is substantially reduced with the slit nozzle (Fig. 8b). It is clear that the new slit nozzle shows more stabilised signals. In fact, the actual quality is better using the slit nozzle than the normal nozzle. When the Ar shielding gas is intentionally reduced with the normal nozzle (Fig. 8c), the OT signal strongly deviates. The shielding gas is expected to blow off the vapour from the melt pool and this effect is weakened when the gas flow is reduced.

The effect of scanning direction is shown in Fig. 9. Here $\theta$ is the angle of processing strip (as shown by the black solid line in Fig. 9a). The scanning direction is normal to $\theta$ (red lines in Fig. 9a). The result indicates that the OT signal becomes unstable at $\theta = 0$ deg and 180 deg, namely when the scanning direction is parallel to the shielding Ar gas flow. In contrast, when $\theta = 90$ deg or 270 deg, the OT signals are smaller and stable, indicating that the processing quality is good. This result will be later discussed with the simulation results.

#### *4.1.2. Data acquisition for simulation: Shielding gas flow and vapour/spatter ejection from melt pool*

In order to use the near-melt-pool information in the simulation as boundary conditions, the velocity field, temperature field and vapour/spatter dynamics are investigated.

**(a) Gas velocity field**

Fig. 10 shows the instantaneous velocity field of the slit nozzle on the XY plane and the YZ plane (see Fig. 2b). Fig. 10a,b,c is for a cold flow without laser heating and Fig. 10d is for laser processing. Fig. 10a,b,c indicates different height from the processing table at 10, 20 and 30 mm. It should be noted that the velocity field is not very much accurately measured in the region close to the nozzle exit (distance of 0–20 mm). At 10 mm (Fig. 10a) inside the slit, the velocity is over 3.2 m/s after the nozzle exit, indicating the fast Ar flow supply. Streak-like velocity defect regions can be seen, which indicate the wakes of the nozzle internal vanes. At 20 mm (Fig. 10b), the streak-like structures still remain slightly and the velocity magnitude is much smaller since the visualised plane is close to the slit wall boundary layer where the wall drag reduces the flow momentum. At 30 mm (Fig. 10c), the visualised plane is out of the nozzle block region and the flow velocity is slow. It means that the slit nozzle can supply a high speed flow but the slit wall may reduce the velocity, and a velocity layer is formed as thick as the nozzle block.

In the hot processing case in Fig. 10d, the velocity increase at the melt pool is observed which is due to vapour ejection. Unfortunately, the very vicinity of the processing plane could not be visualized due to the limitation of the experimental viewing angle. When the scanning direction is toward downstream (Fig. 10d left), the backward-ejected

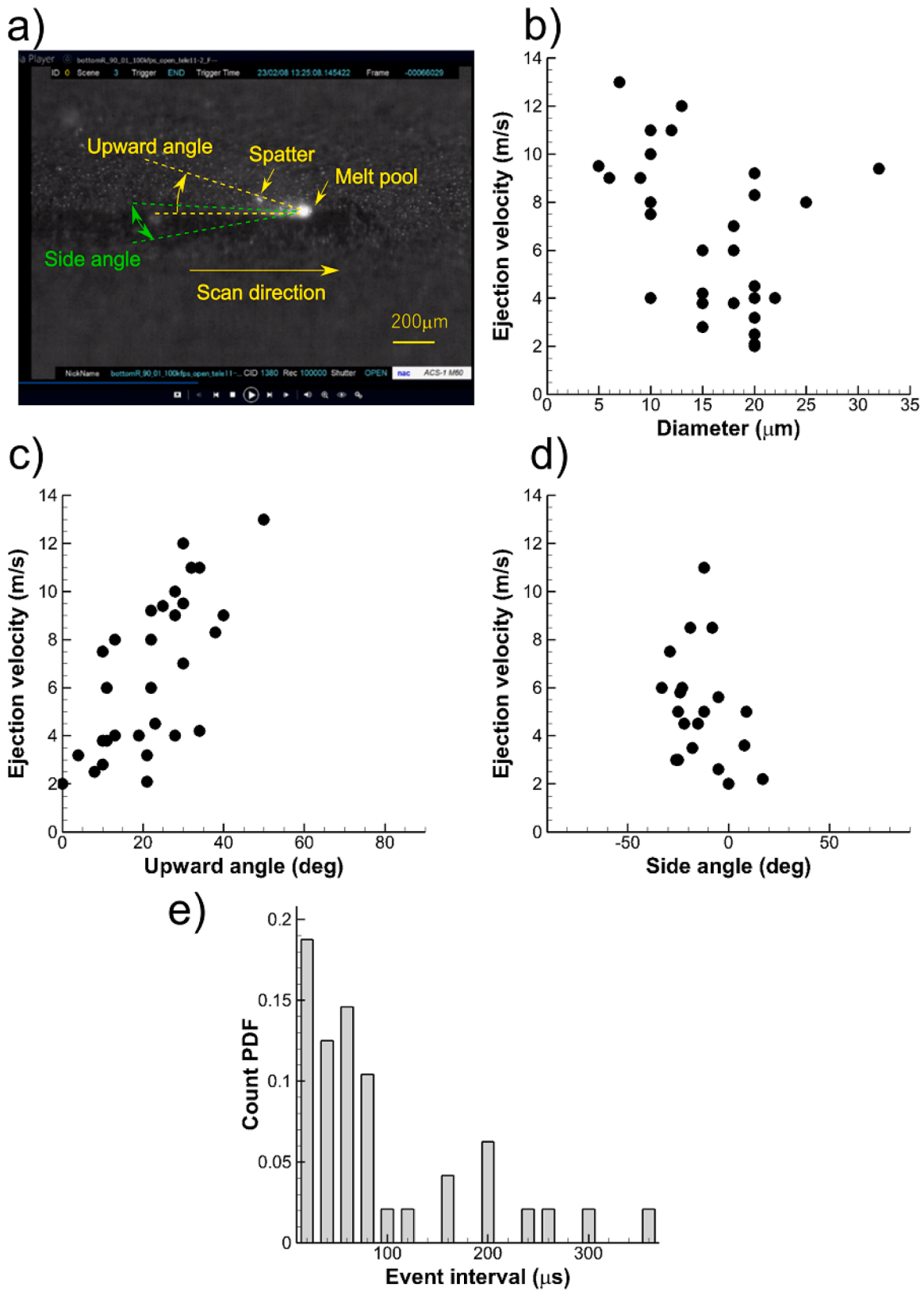


**Fig. 12.** Spatter characteristics. (a) High-speed video image of melt pool and spatter particles, (b) spatter diameter and ejection velocity, (c) upward angle, (d) side angle, and (e) PDF of spatter ejection event time interval. (See **Supplementary Video 3**).

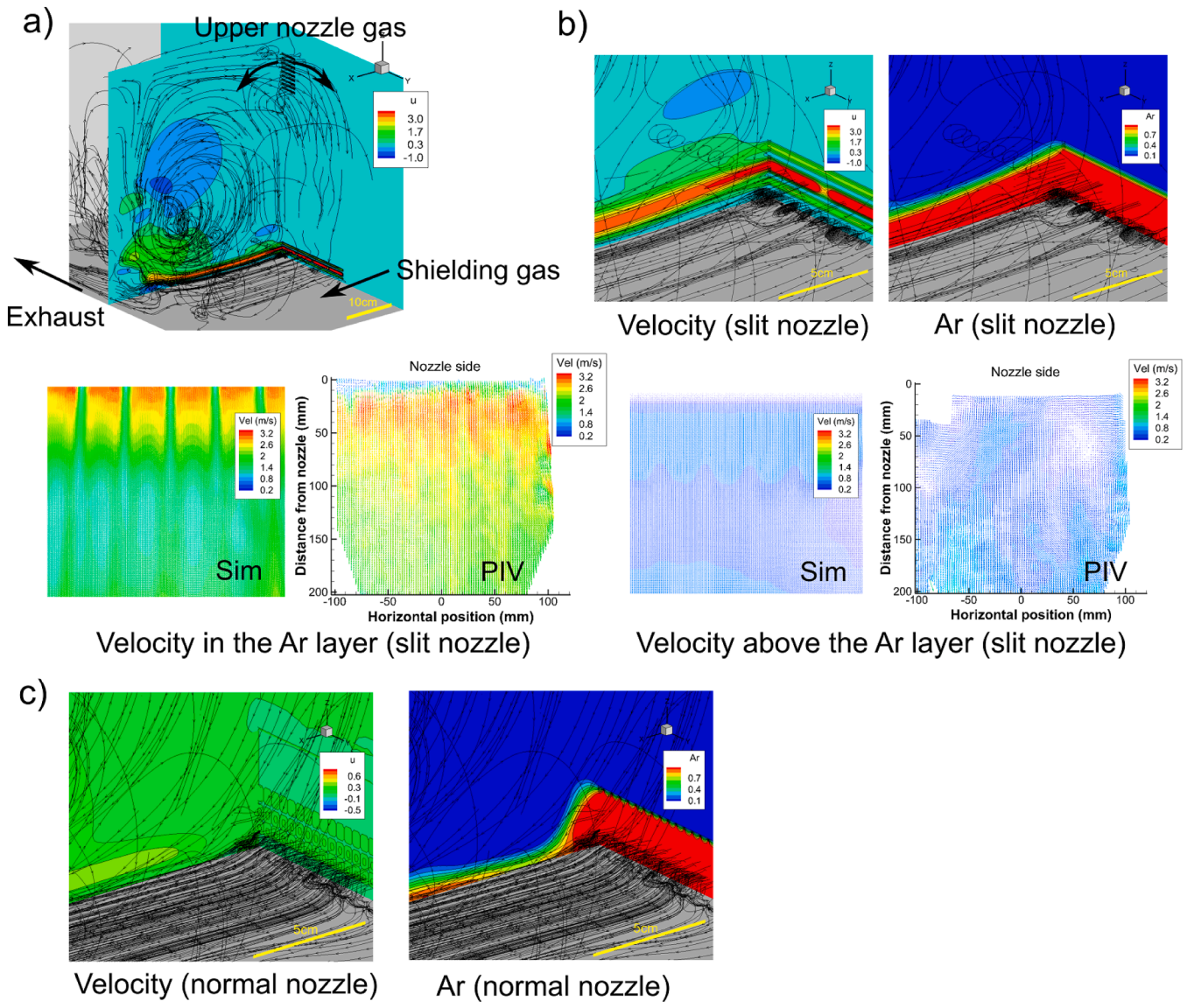


**Fig. 13.** Gas flow field. (a) The overall flow structure (velocity and streamlines), (b) axial velocity and Ar distribution for the slit nozzle (Case B1) and (c) axial velocity and Ar distribution for the normal nozzle (Case B3).

vapour makes a head-on collision with the Ar shielding flow and the velocity magnitude is reduced. Meanwhile, when the scanning direction is toward upstream (Fig. 10d right), the ejected vapour is inclined along the Ar shielding flow and the velocity magnitude is not reduced. The effect of this vapour ejection direction will be later discussed in **4.2.2**. Since the vapour velocity at the root (at the melt pool surface) cannot be directly measured, the spatter velocity will be later utilised to estimate it.

**(b) Temperature field**

The thermal imaging of melt pool gives the surface temperature. Fig. 11 shows an example of $\theta = 90$ deg scanning (the scanning direction is from right to left). The viewing angle is 45 deg from upward. The melt pool can be seen on the surface and backward vapour ejection can be seen especially in the thermal images. Intermittent spatter ejection can be also observed. The temperature is given as a probability density function (PDF) in the upper insert. It should be noted that this PDF plot includes not only the melt pool but the periphery region. The temperature distribution along the green line is also plotted. It is shown that the temperature is mostly stable around 2500–3200 K near the melt pool. This temperature range is consistent with the simulation results shown in Fig. 5. The high temperature region length (nearly equal to the melt pool length) is about 300 μm in the scanning direction. The stable temperature behaviour is related to stable vapour ejection seen in the next subsection.

**(c) Spatter ejection**

The spatter ejection angle and speed are measured using the high-speed video at 100,000 fps. Fig. 12 shows the spatter dynamics extracted from the video. The inclined viewing angle of the camera is compensated in the analysis by using virtual computer graphic images where spatter particles are hypothetically ejected with various ejection angles and comparison with the experimental images at the same viewing angle determines the actual ejection angles. Fig. 12a shows a snapshot of the video where the laser scanning direction is from left to right. A small spatter particle can be seen and it is clear that spatters are ejected backward and upward with some range of spreading angles. The upward angle refers to the angle in the vertically upward direction and the side angle refers to the spreading angle on the processing plane. From Fig. 12b,c,d, the spatter diameter, ejection velocity and the upward and side angles can be identified. They are mostly ejected backward in a certain range of angles. It is speculated that the spatter ejection is due to entrainment by the vapour gas. In the experiment by Yin *et al.* [20] in which a much stronger (max 2000 W) and larger diameter

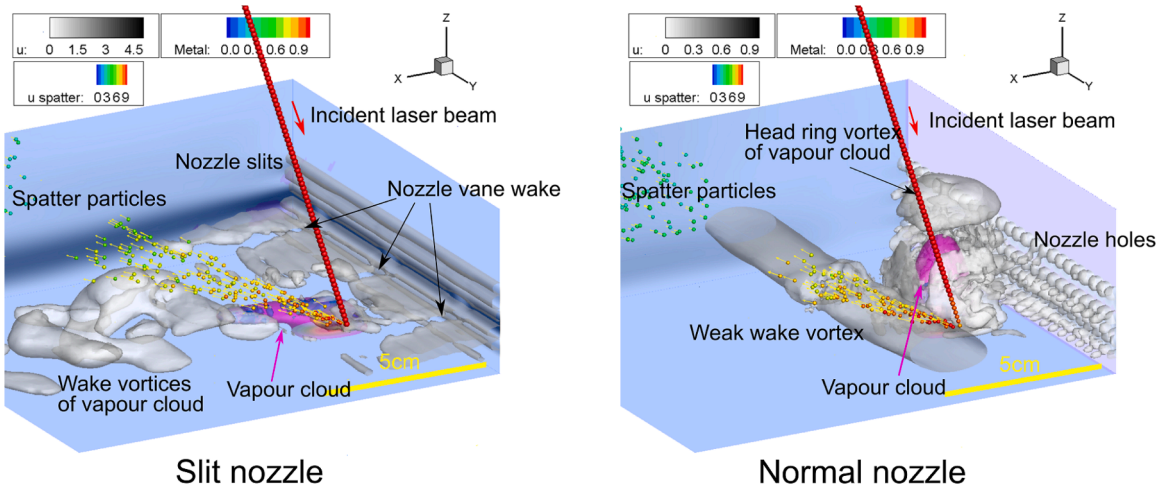


**Fig. 14.** Vortex structure and vapour cloud for the slit and normal nozzles (Cases B1 and B3). The vapour cloud is drawn as a pink iso-surface of the vapour mass fraction of 0.25. The gas phase vortex structures are drawn as gray iso-surfaces. The gas velocity and the spatter velocity are both in m/s. The colour bar (Metal) indicates metal vapour mass fraction.

(318 μm) laser is used, laser interaction with forward-ejected spatters is discussed. Gunenthiram *et al.* [17] also observed that the spatter ejection angle increases (becomes vertical) as the laser power input increases. Under the different process conditions, the present observation is characterised by relatively smaller spatter particles that are mostly ejected backward, quickly going away from the laser region. Therefore, laser-spatter interaction is less likely, although not unhappening. Fig. 12e shows the PDF of time interval between each spatter ejection event. As can be seen, the spatter ejection events occur intermittently. The present result is generally in agreement with Tenbrock *et al.* [4], Yin *et al.* [20,21] and Ly *et al.* [23], for example.

These results are used for the boundary conditions at the melt pool location. The chamber CFD grid does not resolve the melt pool and one grid cell contains the melt pool. To this grid cell, the conditions of spatters are given as boundary conditions. Since the spatter ejection event is hard to set in this scale of CFD simulation in a deterministic way, randomness is introduced. For each value, a probability density function (PDF) is fit from its experimental values in Fig. 12. Then, in the simulation, each event of spatter particle ejection is activated at the time interval determined by the event interval PDF, together with other spatter parameters of diameter, velocity magnitude and angles given by each PDF.

To determine the vapour gas velocity from the melt pool, it is assumed that small (<10 μm) and fast hot spatter particle velocity (~10–14 m/s) represents the gas velocity with the negligible slip velocity. These spatter particles can be seen in the video in Fig. 12 (Supplementary Video 3). Hot spatter particles are self-luminescent and by carefully choosing particles flying straight backward from the melt pool, the temporal motion can be tracked and the flying velocity, and thus the vapour gas velocity, can be obtained. Introducing the randomness in this velocity range, the gas ejection velocity is given as a boundary condition at the melt pool. The plume temperature is given by using the PDF in Fig. 11 with introduced randomness.

### 4.2. Numerical simulation

#### 4.2.1. Shielding gas flow field

From the experimental results in **4.1.1**, it is clear that the shielding gas flow has a significant effect on the processing quality. Therefore, the chamber shielding gas velocity field is investigated. Fig. 13 shows the velocity, streamlines and Ar distribution for Cases B1 and B3. Overall in the chamber scale, the injected Ar gas flows towards the exit exhaust nozzle and part of the flow is rolled up and recirculates toward the front region (Fig. 13a). The upper nozzle serves to partially push the rolled-up flow downward.

The slit nozzle (Case B1) has less nozzle wall drag effect on the Ar flow and the exit velocity is generally faster and the flow is rather straight after injection (Fig. 13b). A small recirculation strip is formed behind the exit step but the entire Ar layer is formed as thick as the nozzle block height. Comparison with the PIV images show good agreement in the structure and the velocity magnitude. Note that the velocity in the region very close to the nozzle cannot be well captured in PIV. The velocity defects (streak-like velocity distribution) are due to the vanes inside the nozzle block. In contrast, for the normal grid (Case B3), the Ar flow after injection is inclined downward toward the processing table below and the Ar layer is thinner. This is due to the reduced injection velocity through the nozzle hole where the nozzle wall viscous force drags the Ar flow substantially, and due to the recirculation zone generated by the backward-facing step at the nozzle exit. Qualitatively, this trend is similar to the velocity field measured by Elkins *et al.* [5] in the same machine chamber of EOS M290. In order to increase the flow rate, the upstream Ar pressure must be increased, but this may be less efficient than using the slit nozzle.

The vapour cloud, vortex structure and laser ray trajectory are shown in Fig. 14. The vapour cloud is drawn as a pink iso-surface of the vapour mass fraction of 0.25. The gas phase vortex structures are drawn as gray iso-surfaces of a $Q$ value, which is the second invariant of the velocity gradient tensor [47], namely

$$Q = \frac{1}{2}\left(\|\mathbf{\Omega}\|^2 - \|\mathbf{S}\|^2\right) \tag{6}$$

where $\Omega_{ij} = \frac{1}{2}\left(\frac{\partial u_i}{\partial x_j} - \frac{\partial u_j}{\partial x_i}\right)$ is the vorticity and $S_{ij} = \frac{1}{2}\left(\frac{\partial u_i}{\partial x_j} + \frac{\partial u_j}{\partial x_i}\right)$ is the strain rate. For a tensor $\mathbf{A}$, $\|\mathbf{A}\|$ denotes $\|\mathbf{A}\| = [\mathrm{tr}(\mathbf{A}\mathbf{A}^t)]^{1/2}$. The scanning direction in Fig. 14 is from downstream toward upstream. The $Q$ value is 7000 $s^{-2}$ for the slit nozzle and 50 $s^{-2}$ for the normal nozzle, respectively, which means the vortex structures in the normal nozzle are weaker.

For the slit nozzle case, sheet-like shear/vortex layers are formed from the nozzle exit due to the inner horizontal slit walls. The observed periodical breaks are due to the vertical inner vanes inside the nozzle. The vortex sheets will generally form two-dimensional (2D) lateral vortices and later break up into three-dimensinal (3D) stuructures. But before the full 3D breakup occurs, the vortex sheets interacts with the ejected vapour. In this case, with the relatively fast Ar flow, the vapour cloud forms a jet-in-crossflow configuration and is deflected toward

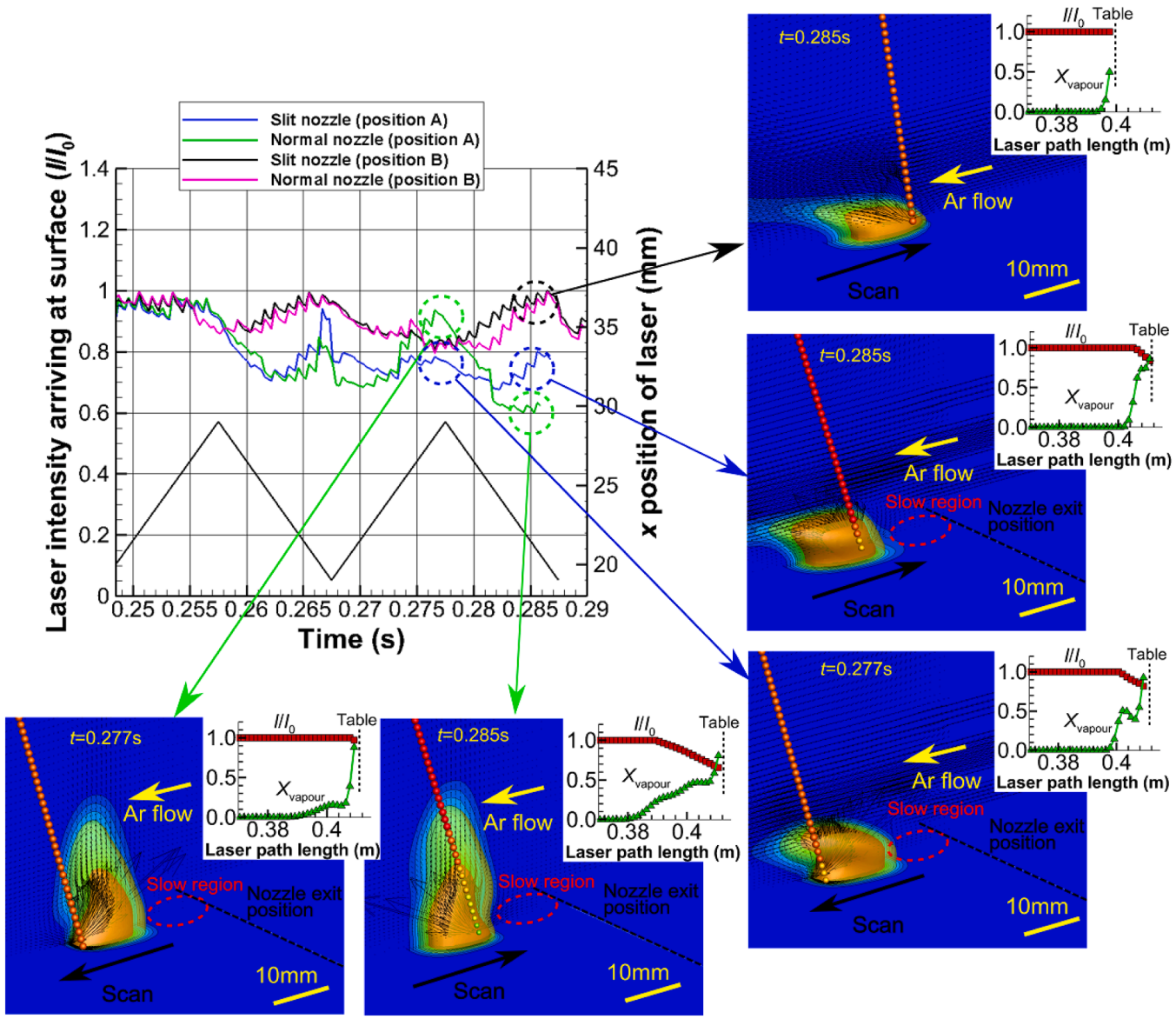


**Fig. 15.** Temporal behaviour of attenuated laser ray energy. Blue: Case B1, green: Case B3, black: Case B2, pink: Case B4. The vapour cloud is drawn by two iso-surfaces of the vapour mass fraction of 0.25 (light green) and 0.5 (orange). The inserts show the laser intensity $I/I_0$ and the vapour mole fraction $X_{vapour}$ along the laser path. The path length is measured from the laser origin. Supplementary Videos S-B1 to S-B4 are provided online.

downstream. After the vapour cloud interaction, wake vortices are formed in the downstream region. In this scanning direction (from downstream to upstrem), the spatters are inclined toward downstream and move away from the melt pool/laser region. Therefore, laser-spatter interaction is not eminent.

For the normal nozzle case, the Ar gas is ejected from nozzle holes and small vortex structures corresponding to each hole can be seen. The overall Ar velocity is slower and the jet-in-crossflow interaction with the vapour cloud is weaker. Therefore, the vapour cloud is rather standing upward and the undisturbed tip of the vapour cloud forms a ring vortex. The Ar flow forms a weak 2D lateral vortex in the wake region, which also indicates a weaker interaction with the vapour cloud. The spatters are similarly inclined toward downstream and move away from the melt pool/laser region, resulting in a weak laser-spatter interaction.

As can be seen, the velocity field is different between the normal nozzle and the slit nozzle, which will critically affect the spatial vapour cloud distribution and thus laser attenuation. In the next subsection, the local field is discussed to see the difference in the laser-fume interaction between the two nozzle configurations in detail.

#### 4.2.2. *Laser-fume and laser-spatter interaction*

**(a) Effect of processing location**

First, the effect of processing location is examined. The scanning direction in this subsection is parallel to the shielding gas flow ($\theta = 0$ deg). Fig. 15 shows the laser ray energy attenuation effect for the two nozzles. In the vapour cloud images, the vapour cloud is drawn by two iso-surfaces of the vapour mass fraction of 0.25 (light green) and 0.5 (orange). The inserts show the laser intensity $I/I_0$ and the vapour mole fraction $X_{vapour}$ along with the laser path. The path distance is measured from the laser origin.

The attenuation is time-dependent and generally, the attenuation is larger at the closer position to the nozzle (position A) and the fluctuation is larger for the normal nozzle. It is also observed that the degree of attenuation generally changes when the scanning direction is reversed. The degree of attenuation is determined by the length of laser trajectory inside the vapour-rich region. Therefore, the vapour shape (of vapour-rich region) and the laser trajectory length inside the vapour cloud determines the attenuation.

At the position A close to the nozzle (Case B1 (slit nozzle: blue) and

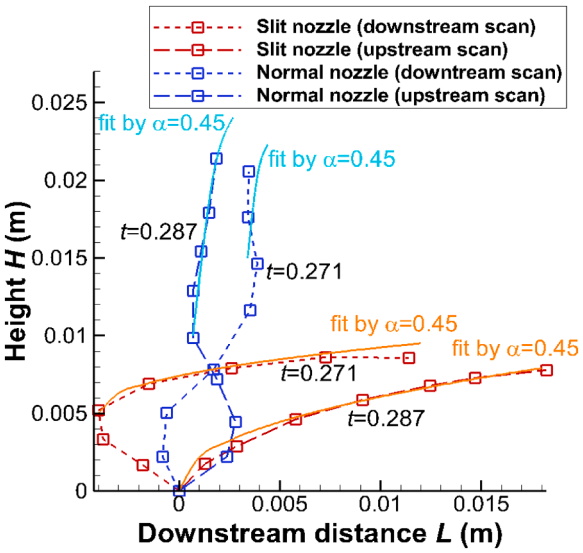


**Fig. 16.** Vapour shape and fitted curves for Cases B1 and B3.

Case B3 (normal nozzle: green)), the attenuation is larger. The ejected vapour is deflected depending on the local Ar flow velocity and the scanning direction. In Case B1, the root part of the vapour cloud stays since a small slow flow region is generated behind the back-facing nozzle exit. The upper part of the vapour cloud is quickly swept away by the faster Ar flow and its height is rather smaller and constant. Therefore, the attenuation is not small but the effect of scanning direction is not very evident.

In contrast, in Case B3 (normal nozzle), the vapour cloud height tends to be much higher. This is due to the relatively slow and thin Ar layer from the nozzle. Since the vapour cloud shape is not flat and the laser is also inclined, the attenuation is affected by the scanning direction. When the scan is toward downstream, the laser trajectory inside the vapour-rich cloud is shorter ($t = 0.274$ s) and the attenuation is smaller. When the scan is toward upstream, the laser trajectory inside the vapour-rich cloud is longer ($t = 0.285$ s) and the attenuation is larger.

Regarding the recirculation zone at the backward-facing step of the nozzle block, which causes the vapour to stay over the processing location, it is generally desired to reduce this effect. This is consistent with the idea of setting an additional nozzle block here to eliminate the step [5]. However, Elkins *et al.* [5] used a multi-hole nozzle block and the drawback of nozzle wall viscous drag for the multi-hole configuration should be carefully considered.

At the side and downstream position B (Cases B2 and B4), the same mechanism works for the vapour cloud shape. But at this position B, the nozzle block step has no effect and the Ar gas velocity exists near the surface. Therefore, the difference in the vapour cloud shape between the normal nozzle and the slit nozzle is smaller. Still, the slit nozzle shows a slightly better result due to relatively faster shielding gas flow.

The vapour cloud height is determined by the momentum ratio of the vapour jet (normal to the shielding flow) to the shielding gas flow [48]. For a typical jet-in-crossflow configuration (for a jet issued exactly perpendicular to the mean outer flow), the vapour height ($H$) has a correlation with the downstream distance from the jet root ($L$) as [48],

$$H/rD \sim (L/rD)^{\alpha} \tag{7}$$

where $D$ is the jet diameter and $\alpha$ is a power factor between 1/3 (=0.33) to 1/2 (=0.5). $r$ is the velocity ratio defined as

$$r = \sqrt{\frac{\rho_v {u_{v\perp}}^2}{\rho_f {u_f}^2 + \rho_v {u_{v//}}^2}} \tag{8}$$

where the subscript $v$ is for the vapour and $f$ is for the Ar gas flow. $\perp$ denotes the normal component and // the parallel component. In this study, the inclined vapour ejection first interacts to offset (or amplify) the mean flow in the lower layer and then interacts with the outer mean flow as a jet in crossflow. Fig. 16 shows the vapour shape and fitted curves for Cases B1 and B3. Except for the lower reversed flow layer region, the upper height evolution follows the correlation of Eq. (7) fitted with $\alpha = 0.45$, with $r = 0.55$ and 0.58 for the slit nozzle and $r = 10.6$ and 19.8 for the normal nozzle. The larger $r$ for the normal nozzle is due to slower Ar flow velocity. Therefore, the vapour cloud dimensions of height and length can be estimated by the Ar flow design. Designing the flow field so that it has a sufficient Ar flow momentum is important to minimise the laser-fume interaction and to assure the fabrication quality, and such a design can be possible by using CFD and the above correlation.

Typical spatter trajectories are shown in Fig. 14. Once these spatter particles are generated, they quickly move away from the vapour region. To have a large effect of laser scattering due to spatter particles, direct hit of the laser beam onto spatter particles flying at some height is frequently needed, which does not occur very often under the present conditions. Therefore, the effect of spatter scattering is limited in terms of laser ray energy attenuation near the melt pool, compared with the laser-fume interaction.

**(b) Effect of scanning direction.**

It is now clear that the vapour cloud shape has a significant effect on laser ray attenuation. Here, the laser scanning direction is changed from parallel ($\theta = 0$ deg) to perpendicular ($\theta = 90$ deg) to the shielding gas flow. The temporal change of laser ray attenuation in Fig. 17 shows that the magnitude of attenuation is slightly smaller and the fluctuation is smaller than $\theta = 0$ deg cases especially in the near nozzle region. This trend is similar to the experimental trend in Fig. 9.

Again, the degree of attenuation at each instant is determined by the length of the laser trajectory inside the vapour-rich cloud. The size of the vapour-rich region indicated by the orange iso-surface becomes larger in the stagnant recirculation zone behind the nozzle (position A), and becomes smaller at the downstream position B where the flow blows vapour away efficiently toward downstream. Still, in contrast to the parallel ($\theta = 0$ deg) scan, the vapour even in the near-nozzle region can be blown rather faster because the vapour will not accumulate consecutively along the scan path under this scanning direction.

Finally, the actual surface-absorbed energy, which is a combination of the laser attenuation and the surface absorptivity, is shown in Fig. 18, using the data of the absorptivity in Fig. 5d [45]. The difference in the absorptivity makes a slight difference among the cases, but the trend is the same as seen above. Generally the energy absorption is better for the perpendicular scan ($\theta = 90$ deg) and for the position B. Also, improvement by the slit nozzle can be seen at the downstream position B.

As seen above, the Ar flow design and the scanning direction strategy are main factors to realise stable processing, by appropriately controlling the vapour plume/fume distribution along the laser. This laser interaction analysis is made possible by considering the chamber-scale flow field and vapour dynamics. This kind of analysis on the direct correlation between the laser ray trajectory and the vapour cloud in AM is the first to be analysed in this study by simulation in a realistic AM chamber. Properly combined experiment and simulation can be a powerful tool to quantitatively design such a flow field in an AM chamber.

The actual phenomena are complicated, and especially the model for solid nano-particles (fume) is still rather rough in this study. Identifying the characteristics and mechanism of generation and possible agglomeration of condensed nano-particles and resultant Mie/Rayleigh scattering may be the next future issue to improve the accuracy of the prediction. Under the conditions investigated, laser-spatter interaction has been found relatively weak due to the ejection mainly in the backward direction. However, spatter ejection characteristics may vary depending on the process conditions. It is important to obtain more data under different conditions.

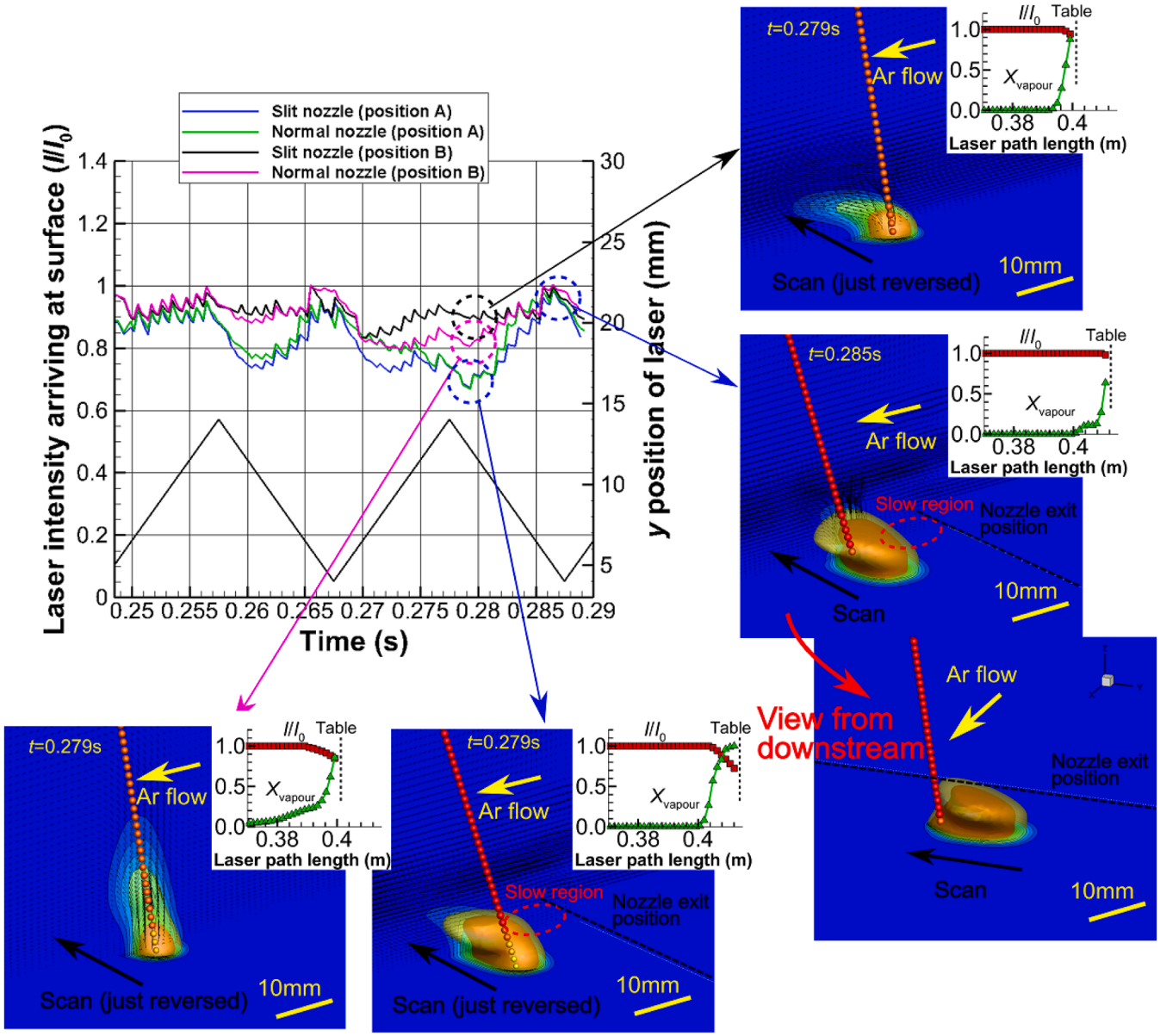


**Fig. 17.** Temporal behaviour of attenuated laser ray energy. Blue: Case C1, green: Case C3, black: Case C2, pink: Case C4. The vapour cloud is drawn by two iso-surfaces of the vapour mass fraction of 0.25 (green) and 0.5 (orange). The inserts show the laser intensity $I/I_0$ and the vapour mole fraction $X_{vapour}$ along the laser path. The path length is measured from the laser origin. Supplementary Videos S-C1 to S-C4 are provided online.

## 5. Conclusions

The effect of shielding gas flow design has been investigated in detail by both experiment and simulation. Specific conclusions can be drawn as follows.

1. The experimental OT signal has a correlation with the melt pool depth. Stronger OT signal means less absorption and the melt pool becomes shallower and vice versa. The difference in the nozzle configuration appears in the OT signal difference, where the newly designed slit nozzle shows better stable results. Intentionally reducing the shielding Ar gas velocity makes the OT signal and the processing quality worse, which indicates that the shielding gas should be sufficiently large. The OT signal also shows the dependence on the scanning angle and the scan perpendicular to the shielding gas flow generally shows better results. Therefore, the shielding gas design is very important and the flow should have a certain magnitude to blow the vapour away.
2. Velocity (of both shielding gas and vapour), temperature and spatters are measured experimentally. Vapour/spatter ejection mostly occurs in the backward direction under the present conditions. The melt pool temperature is reasonably in good agreement with melt pool scale simulation results. The obtained information is used as boundary conditions in the chamber scale simulations.
3. Direct simulation of laser-fume interaction has been conducted for the first time. The simulation results indicate that the shielding gas design has a strong effect on the vapour cloud distribution. To reduce the laser attenuation, the vapour cloud must be quickly blown away by the shielding gas since the laser trajectory distance in the vapour-rich region determines the laser attenuation. The scanning direction is also a factor to determine the vapour distribution. The parallel scan ($\theta = 0$ deg) in the near nozzle region leads to vapour accumulation in the laser region while the perpendicular scan ($\theta = 90$ deg) has a less detrimental effect thanks to blow-off by the shielding gas. The vapour cloud shape can be characterised by the velocity

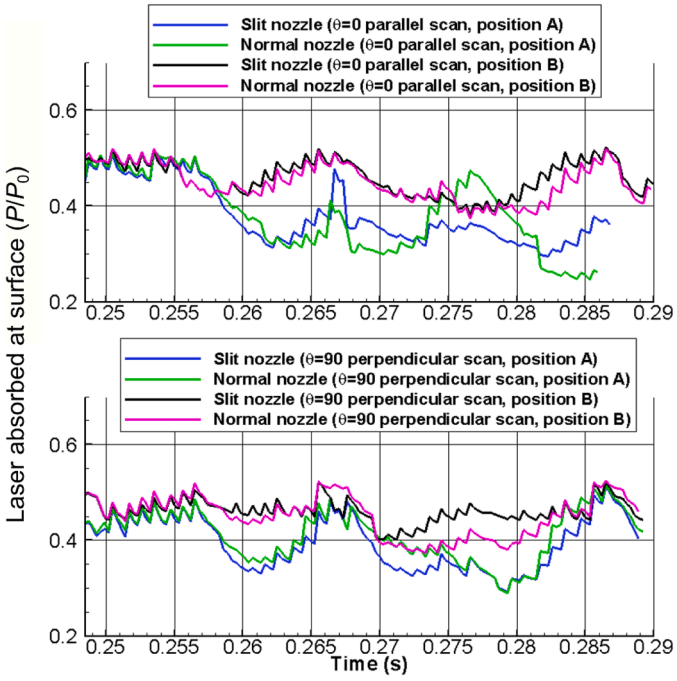


**Fig. 18.** Temporal behaviour of laser energy absorption. The line colour is the same as in Figs. 15 and 17.

(momentum) ratio, as the vapour and the shielding gas comprise the jet-in-crossflow configuration.

The present study has indicated the significance of shielding gas design. In the next step, multi-scale direct simulation connected with the melt pool simulation, especially including the fume (nano-particles) effect, will be considered. Systematic collection of relevant experimental data is also significantly important to widen the applicability of such a predictive method.

## CRediT authorship contribution statement

**Junji Shinjo:** Writing – original draft, Software, Methodology, Investigation, Conceptualization. **Asuka Kutsukake:** Writing – review & editing, Investigation. **Hideki Wakabayashi:** Writing – review & editing, Investigation. **Kazuto Arakawa:** Writing – review & editing, Investigation. **Akira Ogawara:** Writing – review & editing, Visualization, Methodology, Conceptualization. **Hiroyuki Uchida:** Writing – review & editing, Visualization, Methodology, Conceptualization. **Chinnapat Panwisawas:** Writing – review & editing, Investigation, Conceptualization. **Roger C. Reed:** Writing – review & editing.

## Declaration of Competing Interest

The authors declare that they have no known competing financial interests or personal relationships that could have appeared to influence the work reported in this paper.

## Data Availability

Data will be made available on request.

## Acknowledgements

This work was supported by Next Generation TATARA Project sponsored by the Government of Japan and Shimane Prefecture. Experimental support by Seika Digital Image Corp. and NAC Image Technology is greatly acknowledged. Chinnapat Panwisawas acknowledges the funding from Innovation Fellowship by Engineering and Physical Sciences Research Council (EPSRC), UK Research and Innovation (UKRI), under the grant number: EP/S000828/2.

## Appendix

*Numerical simulation methods*

Details of the governing equations in **2.2 Numerical simulation** are presented below.

**A) Shielding gas, vapour dynamics and turbulence equations**.

The numerical simulation is conducted based on the computational fluid dynamics (CFD) approach. As discussed in Section **3.**, the horizontal grid resolution is not small enough to resolve the melt pool. Therefore, the melt pool conditions are given as model boundary conditions. Similarly, unresolved sub-grid scale (SGS) turbulence eddies are modelled in the framework of large eddy simulation (LES).

In the chamber, the continuum phase is comprised of the gas phase. The governing equations are the conservation of mass, momentum, energy and species concentration. The equations are

$$\frac{\partial \rho}{\partial t}+\frac{\partial\left(\rho u_j\right)}{\partial x_j}=S_I \tag{A1}$$

$$\frac{\partial \rho u_i}{\partial t}+\frac{\partial\left(\rho u_i u_j\right)}{\partial x_j}=-\frac{\partial p}{\partial x_i}+\frac{\partial \tau_{ij}}{\partial x_j}+S_{II,i} \tag{A2}$$

$$\frac{\partial E}{\partial t}+\frac{\partial\left(E u_j\right)}{\partial x_j}=-\frac{\partial\left(p u_j\right)}{\partial x_j}-\frac{\partial}{\partial x_j}\left(-\lambda \frac{\partial T}{\partial x_j}\right)+\frac{\partial\left(\tau_{ij} u_i\right)}{\partial x_j}+S_{III} \tag{A3}$$

$$\frac{\partial \rho Y_i}{\partial t}+\frac{\partial\left(\rho Y_i u_j\right)}{\partial x_j}=-\frac{\partial\left(\rho Y_i V_{D,j}\right)}{\partial x_j}+S_I \tag{A4}$$

where $\rho$ is the density, $u_i$ is the velocity component ($u$, $v$, $w$), $p$ is the pressure, $\tau$ is the viscous stress, $E=\rho c_v T+1/2\rho(u^2+v^2+w^2)$ is the total energy, $c_v$ is the specific heat at constant volume, $T$ is the temperature, $\lambda$ is the thermal conductivity for heat conduction by Fourier's law, $Y_i$ is the mass fraction of species $i$ and $V_{D,j}$ is the diffusion velocity formulated by Fick's law. The terms for the interaction with particles $S_I$, $S_{II,i}$ and $S_{III}$ [31] are defined later in **B)**. Finally, the perfect gas equation of state is assumed.

These equations are Favre-filtered (using Favre-averaging $\widetilde{f} = \overline{\rho f}/\overline{\rho}$ where the overbar denotes averaging) to be formulated in LES and the unclosed SGS turbulence terms are modelled by the Smagorinsky model [32]. The subgrid scale (SGS) turbulence term for the momentum equation is the stress term by the eddy viscosity given by

$$\tau_{ij}^{sgs} = -2C_s\overline{\rho}\Delta^2|\widetilde{S}|\widetilde{S}_{ij}$$
$$|\widetilde{S}| = \sqrt{2\widetilde{S}_{ij}\widetilde{S}_{ij}}, \quad \widetilde{S}_{ij} = \frac{1}{2}\left(\frac{\partial\widetilde{u}_i}{\partial x_j} + \frac{\partial\widetilde{u}_j}{\partial x_i}\right) \tag{A5}$$

where $C_s$ is the Smagorinsky constant (=0.1) and $\Delta$ is the filter width (taken as the grid spacing). In Eq. (A5), additional terms for compressible turbulence effects are neglected since the flow velocity is not very fast. The numerical scheme is based on a total-variance diminishing (TVD) scheme using Chakravarthy-Osher's limiter [33]. The viscous and diffusion terms are formulated by the 2nd-order central differencing.

**B) Particle equations**.

Ejected spatter particles are tracked as point-particles in the Lagrangian framework. Collision between spatter particles is not considered here. The spatter (particle) equations are the same as those typically used in particle-laden flows [31],

$$\frac{d\mathbf{x}_d}{dt} = \mathbf{u}_d \tag{A6}$$

$$m_d\frac{d\mathbf{u}_d}{dt} = \mathbf{F} \tag{A7}$$

$$\frac{dm_d}{dt} = -\frac{m_d}{\tau_d}\cdot\frac{Sh}{3Sc}\cdot\ln\left(1+B_M\right) \tag{A8}$$

$$m_d c_{p,d}\frac{dT_d}{dt} = Q + \frac{dm_d}{dt}L \tag{A9}$$

$\mathbf{x}_d$ denotes the particle position and $\mathbf{u}_d$ is the particle velocity. The subscript $d$ denotes the dispersed phase (spatter particles) and $f$ the gas flow around the particle, respectively. $m_d$ is the particle mass, and $\mathbf{F} = m_d f_1/\tau_d\cdot(\mathbf{u}_f - \mathbf{u}_d)$ with $f_1 = C_D Re_d/24$. $C_D$ is the drag coefficient of Stokes drag law for a sphere, namely, $C_D = 24/Re_d$. The particle Reynolds number is $Re_d = |\mathbf{u}_d - \mathbf{u}_f|D_d/\nu_f$, where $\nu_f$ is the flow kinematic viscosity. The Stokes time scale is $\tau_d = \rho_d {D_d}^2/18\mu_f$ and $D_d$ is the particle diameter. The Spalding transfer number is $B_M = (Y_{V,s} - Y_{V,f})/(1 - Y_{V,s})$ and $L$ is the latent heat of vapourisation. The vapour mass fraction at the spatter particle surface $Y_{V,s}$ is assumed to be in the thermal equilibrium with the spatter surface, namely it is determined by the Clapeyron-Clausius relation as $Y_{V,s} = X_{V,s}/(X_{V,s} + (1 - X_{V,s})W_f/W_V)$ with the surface mole fraction $X_{V,s} = {p_f}^{-1}\exp[L/R\cdot({T_B}^{-1} - {T_d}^{-1})]$. $p_f$ is the flow pressure in atm, $T_B$ is the boiling temperature at 1 atm and $R$ is the gas constant. The heat transfer term is modeled as $Q = (m_d Nu/3\tau_d Pr)\cdot c_{p,f} f_2 (T_f - T_d)$ where $c_p$ is the heat capacity at constant pressure, and $f_2 = \beta/(\exp\beta - 1)$ with $\beta = -1.5 Pr\dot{m}_d\tau_d/m_d$. $Sh$, $Nu$, $Sc$ and $Pr$ (=0.74) are the Sherwood, Nusselt, Schmidt and Prandtl numbers, respectively. $Sh$ and $Nu$ are determined by the Ranz-Marshall correlations [31].

The Eulerian-Lagrangian interaction terms ($S_*$) in Eqs. (A1)-(A4) are [31].

$$S_I = \frac{1}{\Delta V}\sum s_1 \tag{A10}$$

$$S_{II,i} = \frac{1}{\Delta V}\frac{1}{\rho}\sum s_{2,i} \tag{A11}$$

$$S_{III} = \frac{1}{\Delta V}\sum s_3 \tag{A12}$$

where $s_1 = -\dot{m}_d$, $s_{2,i} = -(F_i + \dot{m}_d u_{di})$, $s_3 = -[\mathbf{F}\cdot\mathbf{u}_d + Q + \dot{m}_d(0.5|\mathbf{u}_d|^2 + h_{V,s})]$, $\Delta V$ is the grid cell volume and $h_{V,s}$ is the vapour enthalpy. The gas density is assumed to be much smaller than the liquid/solid densities.

The particle equations are numerically solved using the 4th-order Runge-Kutta time integration.

**C) Code validation**.

Physical phenomena related to the present study include convection, species diffusion, heat diffusion and turbulence as indicated in **Appendix A)**. In addition to the direct comparison of the velocity field and the angular laser heat variation trend in **4.2.1**. and **4.2.2.**, code validity is further mentioned. The present code has been applied to many flow field problems and especially combustion cases are the most representative to show the validity since a flame is formed within a balance between species diffusion and heat diffusion (and reaction) under turbulent convection [49–51]. If the code accuracy is not sufficient, unphysical flame quenching (extinction) may occur. In the references [49–51], we have succeeded in conducting validation and reproducing complex physical balances in turbulent flames. See more specific details in each paper. The same code is applied in the present simulation, which assures capturing species and heat diffusion (namely vapour distribution) accurately under turbulent convective conditions.

## Appendix B. Supporting information

Supplementary data associated with this article can be found in the online version at doi:10.1016/j.addma.2020.101681.

## References


[1] B. Ferrar, L. Mullen, E. Jones, R. Stamp, C.J. Sutcliffe, Gas flow effects on selective laser melting (SLM) manufacturing performance, J. Mater. Process. Technol. 212 (2012) 355–364, https://doi.org/10.1016/j.jmatprotec.2011.09.020.

[2] A. Ladewig, G. Schlick, M. Fisser, V. Schulze, U. Glatzel, Influence of the shielding gas flow on the removal of process by-products in the selective laser melting process, Addit. Manuf. 10 (2016) 1–9, https://doi.org/10.1016/j.addma.2016.01.004.

[3] J. Reijonen, A. Revuelta, T. Riipinen, K. Ruusuvuori, P. Puukko, On the effect of shielding gas flow on porosity and melt pool geometry in laser powder bed fusion additive manufacturing, Addit. Manuf. 32 (2020) 101030, https://doi.org/10.1016/j.addma.2019.101030.

[4] C. Tenbrock, T. Kelliger, N. Praetzsch, M. Ronge, L. Jauer, J.H. Schleifenbaum, Effect of laser-plume interaction on part quality in multi-scanner Laser Powder Bed Fusion, Addit. Manuf. 38 (2021) 101810, https://doi.org/10.1016/j.addma.2020.101810.

[5] C.J. Elkins, J. Mireles, H.H. Estrada, D.W. Morgan, H.C. Taylor, R.B. Wicker, Resolving the three-dimensional flow field within commercial metal additive manufacturing machines: application of experimental Magnetic Resonance Velocimetry, Addit. Manuf. 73 (2023) 103651, https://doi.org/10.1016/j.addma.2023.103651.

[6] Z. Snow, L. Scime, A. Ziabari, B. Fisher, V. Paquit, Observation of spatter-induced stochastic lack-of-fusion in laser powder bed fusion using in situ process monitoring, Addit. Manuf. 61 (2023) 103298, https://doi.org/10.1016/j.addma.2022.103298.

[7] X. Zhang, B. Cheng, C. Tuffile, Simulation study of the spatter removal process and optimization design of gas flow system in laser powder bed fusion, Addit. Manuf. 32 (2020) 101049, https://doi.org/10.1016/j.addma.2020.101049.

[8] C.-Y. Chien, T.-N. Le, Z.-H. Lin, Y.-L. Lo, Numerical and experimental investigation into gas flow field and spattering phenomena in laser powder bed fusion processing of Inconel 718, Mater. Des. 210 (2021) 110107, https://doi.org/10.1016/j.matdes.2021.110107.

[9] J. Zou, W. Yang, S. Wu, Y. He, R. Xiao, Effect of plume on weld penetration during high-power fiber laser welding, J. Laser Appl. 28 (2016) 022003, https://doi.org/10.2351/1.4940148.

[10] H. Zheng, H. Li, L. Lang, S. Gong, Y. Ge, Effects of scan speed on vapor plume behavior and spatter generation in laser powder bed fusion additive manufacturing, J. Manuf. Process. 36 (2018) 60–67, https://doi.org/10.1016/j.jmapro.2018.09.011.

[11] J. Ye, S.A. Khairallah, A.M. Rubenchik, M.F. Crumb, G. Guss, J. Belak, M. J. Matthews, Energy coupling mechanisms and scaling behavior associated with laser powder bed fusion additive manufacturing, Adv. Eng. Mater. 21 (2019) 1900185, https://doi.org/10.1002/adem.201900185.

[12] S.A. Khairallah, A.A. Martin, J.R.I. Lee, G. Guss, N.P. Calta, J.A. Hammons, M. H. Nielsen, K. Chaput, E. Schwalbach, M.N. Shah, M.G. Chapman, T.M. Willey, A. M. Rubenchik, A.T. Anderson, Y.M. Wang, M.J. Matthews, W.E. King, Controlling interdependent meso-nanosecond dynamics and defect generation in metal 3D printing, Science 368 (2020) 660–665, https://doi.org/10.1126/science.aay7830.

[13] H. Zheng, Y. Wang, Y. Xie, S. Yang, R. Hou, Y. Ge, L. Lang, S. Gong, H. Li, Observation of vapor plume behavior and process stability at single-track and multi-track levels in laser powder bed fusion regime, Metals 11 (2021) 937, https://doi.org/10.3390/met11060937.

[14] P. Bidare, I. Bitharas, R.M. Ward, M.M. Attallah, A.J. Moore, Fluid and particle dynamics in laser powder bed fusion, Acta Mater. 142 (2018) 107–120, https://doi.org/10.1016/j.actamat.2017.09.051.

[15] P. Bidare, I. Bitharas, R.M. Ward, M.M. Attallah, A.J. Moore, Laser powder bed fusion in high-pressure atmospheres, Int. J. Adv. Manuf. Technol. 99 (2018) 543–555, https://doi.org/10.1007/s00170-018-2495-7.

[16] Q. Guo, C. Zhao, L.I. Escano, Z. Young, L. Xiong, K. Fezzaa, W. Everhart, B. Brown, T. Sun, L. Chen, Transient dynamics of powder spattering in laser powder bed fusion additive manufacturing process revealed by in-situ high-speed high-energy x-ray imaging, Acta Mater. 151 (2018) 169–180, https://doi.org/10.1016/j.actamat.2018.03.036.

[17] V. Gunenthiram, P. Peyre, M. Schneider, M. Dal, F. Coste, I. Koutiri, R. Fabbro, Experimental analysis of spatter generation and melt-pool behavior during the powder bed laser beam melting process, J. Mater. Process. Tech. 251 (2018) 376–386, https://doi.org/10.1016/j.jmatprotec.2017.08.012.

[18] Z.A. Young, Q. Guo, N.D. Parab, C. Zhao, M. Qu, L.I. Escano, K. Fezzaa, W. Everhart, T. Sun, L. Chen, Types of spatter and their features and formation mechanisms in laser powder bed fusion additive manufacturing process, Addit. Manuf. 36 (2020) 101438, https://doi.org/10.1016/j.addma.2020.101438.

[19] I. Bitharas, A. Burton, A.J. Ross, A.J. Moore, Visualisation and numerical analysis of laser powder bed fusion under cross-flow, Addit. Manuf. 37 (2021) 101690, https://doi.org/10.1016/j.addma.2020.101690.

[20] J. Yin, D. Wang, L. Yang, H. Wei, P. Dong, L. Ke, G. Wang, H. Zhu, X. Zeng, Correlation between forming quality and spatter dynamics in laser powder bed fusion, Addit. Manuf. 31 (2020) 100958, https://doi.org/10.1016/j.addma.2019.100958.

[21] J. Yin, D. Wang, H. Wei, L. Yang, L. Ke, M. Hu, W. Xiong, G. Wang, H. Zhu, X. Zeng, Dual-beam laser-matter interaction at overlap region during multi-laser powder bed fusion manufacturing, Addit. Manuf. 46 (2021) 102178, https://doi.org/10.1016/j.addma.2021.102178.

[22] I. Bitharas, N. Parab, C. Zhao, T. Sun, A.D. Rollett, A.J. Moore, The interplay between vapour, liquid, and solid phases in laser powder bed fusion, Nat. Commun. 13 (2022) 2959, https://doi.org/10.1038/s41467-022-30667-z.

[23] S. Ly, A.M. Rubenchik, S.A. Khairallah, G. Guss, M.J. Matthews, Metal vapor micro-jet controls material redistribution in laser powder bed fusion additive manufacturing, Sci. Rep. 7 (2017) 4085, https://doi.org/10.1038/s41598-017-04237-z.

[24] X. Li, C. Zhao, T. Sun, W. Tan, Revealing transient powder-gas interaction in laser powder bed fusion process through multi-physics modeling and high-speed synchrotron x-ray imaging, Addit. Manuf. 35 (2020) 101362, https://doi.org/10.1016/j.addma.2020.101362.

[25] X. Li, Q. Guo, L. Chen, W. Tan, Quantitative investigation of gas flow, powder-gas interaction, and powder behavior under different ambient pressure levels in laser powder bed fusion, Int. J. Mach. Tools Manuf. 170 (2021) 103797, https://doi.org/10.1016/j.ijmachtools.2021.103797.

[26] H. Chen, W. Yan, Spattering and denudation in laser powder bed fusion process: multiphase flow modelling, Acta Mater. 196 (2020) 154–167, https://doi.org/10.1016/j.actamat.2020.06.033.

[27] J. Liu, P. Wen, Metal vaporization and its influence during laser powder bed fusion process, Mater. Des. 215 (2022) 110505, https://doi.org/10.1016/j.matdes.2022.110505.

[28] Z. Li, H. Li, J. Yin, Y. Li, Z. Nie, X. Li, D. You, K. Guan, W. Duan, L. Cao, D. Wang, L. Ke, Y. Liu, P. Zhao, L. Wang, K. Zhu, Z. Zhang, L. Gao, L. Hao, A review of spatter in laser powder bed fusion additive manufacturing: in situ detection, generation, effects, and countermeasures, Micromachines 13 (2022) 1366, https://doi.org/10.3390/mi13081366.

[29] EOS M290, EOS GmbH, https://www.eos.info/en/industrial-3d-printer/metal/eos-m-290.

[30] E.O.S. Nickel Alloy IN718 Material Data Sheet, EOS GmbH, https://www.eos.info/03_system-related-assets/material-related-contents/metal-materials-and-examples/metal-material-datasheet/nickelalloy-inconel/material_datasheet_eos_nickelalloy_in718_01-23_en.pdf.

[31] N.A. Okong'o, J. Bellan, Consistent large-eddy simulation of a temporal mixing layer laden with evaporating drops. Part 1. Direct numerical simulation, formulation and a priori analysis, J. Fluid Mech. 499 (2004) 1–47, https://doi.org/10.1017/S0022112003007018.

[32] J. Smagorinsky, General circulation experiment with primitive equations", Mon. Weather Rev. 91 (1963) 99–164, https://doi.org/10.1175/1520-0493(1963)091<0099:GCEWTP>2.3.CO;2.

[33] S. Chakravarthy, S. Osher, A new class of high accuracy TVD schemes for hyperbolic conservation laws, AIAA Pap. 1985-363 (1985), https://doi.org/10.2514/6.1985-363.

[34] C. Panwisawas, Y.T. Tang, R.C. Reed, Metal 3D printing as a disruptive technology for superalloys, Nat. Commun. 11 (2020) 2327, https://doi.org/10.1038/s41467-020-16188-7.

[35] J. Xu, Y. Luo, L. Zhu, J. Han, C. Zhang, D. Chen, Effect of shielding gas on the plasma plume in pulsed laser welding, Measurement 134 (2019) 25–32, https://doi.org/10.1016/j.measurement.2018.10.047.

[36] Y. Zhang, F. Wang, J. Liu, J. Sun, Simulation of the inverse bremsstrahlung absorption by plasma plume in laser penetration welding, Chem. Phys. Lett. 793 (2022) 139434, https://doi.org/10.1016/j.cplett.2022.139434.

[37] R.B. Miles, W.R. Lempert, J.N. Forkey, Laser Rayleigh scattering Meas, Sci. Technol. 12 (2001) R33–R51, https://doi.org/10.1088/0957-0233/12/5/201.

[38] P.Yu Shcheglov, S.A. Uspenskiy, A.V. Gumenyuk, V.N. Petrovskiy, M. Rethmeier, V.M. Yermachenko, Plume attenuation of laser radiation during high power fiber laser welding, Laser Phys. Lett. 8 (2011) (2011) 475–480, https://doi.org/10.1002/lapl.201110010.

[39] G. Mie, Beiträge zur Optik trüber Medien, speziell kolloidaler Metallösungen, Ann. der Phys. 330 (1908) 377–445, https://doi.org/10.1002/andp.19083300302.

[40] C.F. Bohren, D. Huffman, Absorption and scattering of light by small particles. Wiley Science Paperback Series, Wiley, 1998. https://doi.org/10.1002/9783527618156.

[41] J. Shinjo, C. Panwisawas, Digital materials design by thermal-fluid science for multi-metal additive manufacturing, Acta Mater. 210 (2021) 116825, https://doi.org/10.1016/j.actamat.2021.116825.

[42] C. Panwisawas, Y. Gong, Y.T. Tang, R.C. Reed, J. Shinjo, Additive manufacturability of superalloys: process-induced porosity, cooling rate and metal vapour, Addit. Manuf. 47 (2021) 102339, https://doi.org/10.1016/j.addma.2021.102339.

[43] J. Shinjo, C. Panwisawas, Chemical species mixing during direct energy deposition of bimetallic systems using titanium and dissimilar refractory metals for repair and biomedical applications, Addit. Manuf. 51 (2022) 102654, https://doi.org/10.1016/j.addma.2022.102654.

[44] J. Shinjo, A. Kutsukake, A. Arote, Y.T. Tang, D.G. McCartney, R.C. Reed, C. Panwisawas, Physics-based thermal-chemical-fluid-microstructure modelling of in-situ alloying using additive manufacturing: Composition-microstructure control, Addit. Manuf. 64 (2023) 103428, https://doi.org/10.1016/j.addma.2023.103428.

[45] M. Khorasani, A. Ghasemi, M. Leary, E. Sharabian, L. Cordova, I. Gibson, D. Downing, S. Bateman, M. Brandt, B. Rolfe, The effect of absorption ratio on meltpool features in laser-based powder bed fusion of IN718, Opt. Laser Technol. 153 (2022) 108263, https://doi.org/10.1016/j.optlastec.2022.108263.

[46] H. Wang, Y. Zhang, K. Chen, Modeling of temperature distribution in laser welding of lapped martensitic steel M1500 and softening estimation, J. Manuf. Sci. Eng. 138 (2016) 111006, https://doi.org/10.1115/1.4033391.

[47] J. Jeong, F. Hussain, On the identification of a vortex, J. Fluid Mech. 285 (1995) 69–94, https://doi.org/10.1017/S0022112095000462.

[48] J. Shinjo, J. Xia, L.C. Ganippa, A. Megaritis, Puffing-enhanced fuel/air mixing of an evaporating n-decane/ethanol emulsion droplet and a droplet group under

convective heating, J. Fluid Mech. 793 (2016) 444–476, https://doi.org/10.1017/jfm.2016.130.
[49] Y. Mizobuchi, S. Tachibana, J. Shinjo, S. Ogawa, T. Takeno, A numerical analysis of the structure of turbulent hydrogen jet lifted flame, Proc. Combust. Inst. 29 (2002) 2009–2015, https://doi.org/10.1016/S1540-7489(02)80245-0.
[50] Y. Mizobuchi, J. Shinjo, S. Ogawa, T. Takeno, A numerical study on the formation of diffusion flame islands in a turbulent hydrogen jet lifted flame, Proc. Combust. Inst. 30 (2005) 611–619, https://doi.org/10.1016/j.proci.2004.08.142.
[51] J. Shinjo, S. Matsuyama, Y. Mizobuchi, S. Ogawa, Study on flame dynamics with secondary fuel injection control by large eddy simulation, Combust. Flame 150 (2007) 277–291, https://doi.org/10.1016/j.combustflame.2007.01.011.